

# Tracing the envelopes around embedded low-mass young stellar objects with $\text{HCO}^+$ and millimeter-continuum observations

Michiel R. Hogerheijde and Ewine F. van Dishoeck

Sterrewacht Leiden, P.O. Box 9513, 2300 RA Leiden, The Netherlands

Geoffrey A. Blake

Division of Geological and Planetary Sciences, California Institute of Technology, MS 150–21,  
Pasadena, CA 91125

and

Huib Jan van Langevelde

Joint Institute for VLBI in Europe, P.O. Box 2, 7990 AA, Dwingeloo, The Netherlands

## ABSTRACT

The envelopes and disks around embedded low-mass young stellar objects (YSOs) are investigated through millimeter continuum and  $\text{HCO}^+$  line emission. Nine sources, selected on the basis of their  $\text{HCO}^+$  3–2 emission from an IRAS flux- and color-limited sample of 24 objects, are observed in  $\lambda = 3.4$  and 2.7 mm continuum emission with the Owens Valley Millimeter Array, and in the  $\text{HCO}^+$  and  $\text{H}^{13}\text{CO}^+$  4–3, 3–2, and 1–0 transitions at the James Clerk Maxwell and IRAM 30m telescopes. All nine sources are detected at 3.4 and 2.7 mm in the interferometer beam, with total fluxes between 4 and 200 mJy. The visibilities can be fit with an unresolved ( $< 3''$ ) point source, and, in about half of the sources, with an extended envelope. The point sources, presumably thermal dust emission from circumstellar disks, typically contribute 30–75% of the continuum flux observed at 1.1 mm in a  $19''$  beam, assuming a spectral slope of 2.5. The fact that at least two-thirds of our sources show point-source emission indicates that circumstellar disks are established early in the embedded phase. The remainder of the 1.1 mm single dish flux is attributed to an extended envelope, with a mass of 0.001–0.26  $M_{\odot}$  within a  $19''$  beam. In  $\text{HCO}^+$ , the  $J=1-0$  line is seen to trace the surrounding cloud, while the emission from  $J=3-2$  and 4–3 is concentrated toward the sources. All sources look marginally resolved in these lines, indicative of a power-law brightness distribution. A beam-averaged  $\text{HCO}^+$  abundance of  $(1.2 \pm 0.4) \times 10^{-8}$  with respect to  $\text{H}_2$  is derived.

The 1.1 mm continuum fluxes and  $\text{HCO}^+$  line intensities of the envelopes correlate well, and are modeled with the simple inside-out collapse model of Shu (1977) and with power-law density distributions of slopes  $p = 1-3$ . All models provide satisfactory fits to the observations, indicating that  $\text{HCO}^+$  is an excellent tracer of the envelopes. Of the 15 sources of the original sample that were either undetected in  $\text{HCO}^+$  3–2

or too weak to be selected, seven show 1.1 mm single-dish fluxes comparable to our objects. It is proposed that all of the 1.1 mm flux of the former sources should be attributed to compact circumstellar disks. The relative evolutionary phase of a YSO, defined as the current ratio of stellar mass over envelope mass, is traced by the quantity  $\int T_{\text{mb}} dV(\text{HCO}^+ 3-2) / L_{\text{bol}}$ . Sources which are undetected in  $\text{HCO}^+$  are found to have significantly lower values in this tracer than do the objects of our subsample, indicating that the former objects are more evolved. The sources which are weak in  $\text{HCO}^+ 3-2$  are indistinguishable from our subsample in this tracer, and have intrinsically low masses. It is concluded that  $\text{HCO}^+$ , especially in its 3–2 and 4–3 transitions, is a sensitive tracer of the early embedded phase of star formation.

*Subject headings:* ISM: abundances — ISM: molecules — stars: formation — stars: low-mass, brown dwarfs — stars: pre-main sequence

## 1. Introduction

Low-mass protostars spend the earliest stages of their evolution embedded in large amounts of gas and dust. These envelopes are dispersed over the course of a few times  $10^5$  yr, after which the pre-main-sequence object, possibly surrounded by an accretion disk or its remnant, is revealed at near-infrared and optical wavelengths. Even though the general characteristics of this evolution are well understood (see Shu et al. 1993 for a recent overview), many details remain uncertain. During the early embedded phase, various physical processes occur simultaneously within a few thousand AU of the forming star. These include the formation and evolution of a circumstellar disk, accretion of matter onto the protostar, the onset of an outflow, and the dissipation of the envelope. The evolution of these phenomena is best studied by observing a well-defined sample of low-mass young stellar objects (YSOs), and by probing all components of their environment on the relevant spatial scales.

Several surveys of the (sub-) millimeter continuum emission of various classes of YSOs have been undertaken in recent years using single-dish telescopes (e.g., Beckwith et al. 1990, Barsony & Kenyon 1992, Moriarty-Schieven et al. 1994, André & Montmerle 1994, Osterloh & Beckwith 1995). These studies have established that  $\sim 60\%$  of T Tauri stars (class II objects; Lada 1987) have circumstellar disks, and that the mass of these disks decreases over a period of a few times  $10^6$  yr. The interpretation of such data in the earlier embedded phase (class I) is much more ambiguous, since, in addition to the disks, the envelopes also contribute to the observed single-dish flux. During the embedded phase, matter is transferred from the envelope to the (growing) disk. Since the latter is likely to be optically thick even at millimeter wavelengths the spectral slope of its emission is determined by geometry and orientation, and only lower limits of its mass can be inferred. The high spatial resolution offered by interferometer observations is essential to separate the relative contributions of disk and envelope, as demonstrated by Keene & Masson

(1990), Terebey, Chandler & André (1993) and Butner, Natta & Evans (1994). Circumstellar disks have been tentatively resolved for only a few embedded objects, with typical semi-major axes of 60–80 AU (L1551 IRS 5, HL Tau: Lay et al. 1994; T Tau: van Langevelde, van Dishoeck & Blake 1995; L1551 IRS 5: Mundy et al. 1996). Caution in the interpretation of these limited interferometry data is urged, since the recent results of Looney et al. (1996) show that the allegedly resolved disk around L1551 IRS 5 is in fact a binary, with each component surrounded by an unresolved disk.

An alternative approach for studying circumstellar envelopes is to use spectral line observations to test models of cloud collapse such as those developed by Shu (1977), Terebey, Shu & Cassen (1984), Galli & Shu (1993), Fiedler & Mouschovias (1992), (1993), Boss (1993), and Foster & Chevalier (1993). Whereas the continuum data are only sensitive to the total mass in the beam, line observations also test the density and velocity structure. Detailed calculations of the molecular excitation and radiative line transfer in model envelopes have been performed by Zhou (1992, 1995), Zhou et al. (1993), Walker, Narayanan & Boss (1994), and Choi et al. (1995), but comparison with observations has been limited to a few specific, very young class 0 objects such as B335 and IRAS 16293–2422. Although the results seem to be consistent with the simple inside-out collapse models of Shu (1977) and Terebey et al. (1984), the models have not yet been tested over the entire time span of the embedded phase. Ohashi et al. (1991, 1996) and Moriarty-Schieven et al. (1992, 1995) have surveyed a large sample of embedded objects using various transitions of the CS molecule to probe a range of excitation conditions. This molecular approach works best if the abundance of the adopted species does not change with time through, e.g., depletion, and if it uniquely traces the envelope but none of the other components. As will be shown in this work, the HCO<sup>+</sup> ion may be better suited for this purpose than CS.

There are several observational developments which make the detailed study of a larger sample timely. First, millimeter interferometers have expanded in size over the last few years, increasing both the sensitivity and mapping speed by large factors. Second, single-dish submillimeter telescopes have been equipped with low-noise SIS detectors at high frequencies, which makes observations of the less massive, presumably more evolved, envelopes feasible. Third, powerful bolometer arrays to trace the continuum emission from dust are just coming on line.

Stimulated by the availability of these new techniques, we have carried out a detailed study of nine embedded low-mass YSOs in the nearby (140 pc) Taurus–Auriga star-forming region, using both single dish and interferometric techniques. These objects span a large range in luminosity and outflow activity, presumably reflecting variations in age and mass. Both continuum emission and a variety of molecular transitions have been observed, tracing densities from  $10^4$  to  $10^8$  cm<sup>-3</sup>, temperatures between 10 and 150 K, and angular scales of 3'' to 2' (400 AU to 15,000 AU at 140 pc), independent of orientation. This large range in probed physical conditions and scales, achieved through the combination of single-dish and interferometer observations, distinguishes our work from most studies mentioned above.

The aim of this paper, the first in a series, is to investigate the evolution of the mass and density structure of the envelope using both continuum and line observations. The results will be tested against one of the simplest models of protostellar collapse (Shu 1977), and closely related power-law density distributions. A second objective is to investigate whether even the most embedded YSOs are already surrounded by circumstellar disks. Ohashi et al. (1996) found that only a small fraction,  $\sim 15\%$ , of the embedded objects shows compact 98 GHz emission in the Nobeyama interferometer. Compared to the number of T Tauri stars with disks, this detection rate is low, and has been interpreted as an indication of disk growth during the embedded phase. A final objective is to study the usefulness of certain molecules, especially  $\text{HCO}^+$ , as reliable tracers of the circumstellar environment. This is important not only for constraining the physical structure, but also for establishing a baseline for future studies of the chemical evolution.

The choice of the Taurus–Auriga region is motivated by its close proximity, the relative isolation in which its YSOs appear to form, and the extensive literature on this region including the objects of our sample (see references throughout this paper). By focusing on a single star-forming region, the effects of different environment are minimized. Systematic infrared and millimeter surveys of Taurus have identified most of the embedded class I objects in this cloud down to 1 mm fluxes of 10 mJy, corresponding to envelope masses of  $0.0015 M_{\odot}$  (Tamura et al. 1991, Ohashi et al. 1996). As a subset of this complete sample, our nine objects are well defined and representative of the embedded phase.

The outline of the paper is as follows. In §2 the nine sources studied in this paper are introduced, together with their selection from the sample defined by Tamura et al. (1991). The observations are discussed in §3. In §4 the millimeter-continuum emission of the disks and envelopes around the sources are analyzed. The interferometer observations and literature values of the 1.1 mm single-dish fluxes are used to obtain ‘pure’ envelope fluxes. The results of the  $\text{HCO}^+$  observations are presented in §5, and further analyzed together with the envelope fluxes within the framework of the spherically symmetric inside-out collapse model of Shu (1977) and related power-law density distributions in §6. The implications for the full sample of Tamura et al. (1991) are discussed in §7, where a relative evolutionary ordering of the objects is proposed. Our main conclusions are summarized in §8.

## 2. Source sample

Our sources have been chosen from the flux- and color-limited sample of 24 IRAS sources located in Taurus–Auriga identified as embedded YSOs by Tamura et al. (1991, hereafter TGWW). Their main selection criteria are infrared color  $\log[F_{\nu}(25 \mu\text{m})/F_{\nu}(60 \mu\text{m})] < -0.25$ , and infrared flux  $F_{\nu} > 5 \text{ Jy}$  at either 60 or 100  $\mu\text{m}$ . Sources with a known identification as an SAO star or a galaxy were rejected. In Table 2 the sources of TGWW are listed with some of their properties. One source (04154+1755) is listed as a galaxy in the SIMBAD database, and is dropped from the sample. The color criterion limits the sources to objects more embedded than the majority

of T Tauri stars; only eight out of 23 are optically visible T Tauri-like objects. The bolometric luminosity of the sample ranges between 0.7 and 22  $L_{\odot}$ . Near-infrared imaging of the sample by TGWW and Kenyon et al. (1993b) shows that most sources have associated reflection nebulosity with sizes between 1000 and 3000 AU. Seven out of the 23 sources have a clear monopolar or bipolar morphology, suggesting that the bipolar outflow plays an important role in the appearance of YSOs at these short wavelengths. CO outflow emission is detected toward 20 out of the 23 objects (Moriarty-Schieven et al. 1994).

One source, Haro 6–10 (04263+2426; identified with GV Tau = Elias 3–7, located in the L1524 cloud), was added to this sample following Kenyon, Calvet & Hartmann (1993a) and Leinert & Haas (1989). The latter authors show that this object is a T Tauri star (GV Tau) with a more embedded companion. Its 25–60  $\mu\text{m}$  color index of  $-0.19$  is only just above the selection criterion of TGWW.

Fourteen of the 24 objects of the sample were found to show  $\text{HCO}^+$  3–2 emission of  $T_{\text{mb}} > 0.5$  K in the 19'' beam of the James Clerk Maxwell Telescope (see §3.2, Fig. 1, and Table 2). The nine strongest of these objects were subsequently selected for our subsample, and are listed in Table 1 with some of their basic properties. Seven are embedded sources (class I according to the classification of Lada 1987); T Tau and Haro 6–10 (GV Tau) are optically visible (class II), but have more embedded companions. All nine show evidence of CO outflow emission (Terebey, Vogel & Myers 1989; Moriarty-Schieven et al. 1994; Hogerheijde et al. 1998a). It should be kept in mind that, given the observed binary frequency of T Tauri stars of 40–60% (Ghez et al. 1993; Leinert et al. 1993), four to six of our nine sources may in fact be multiple systems. In addition to Haro 6–10 and T Tau (Dyck, Simon & Zuckerman 1982; Ghez et al. 1993), companions have been reported for L1551 IRS 5 (Looney et al. 1996) and L1527 IRS (Fuller, Ladd & Hodapp 1996).

The pointing centers of our observations were based on optical or near-infrared observations, which have an accuracy of 2''–3''. Because of its deeply embedded nature, no reliable position of L1527 IRS was available, and the IRAS position was used. In Table 1 the positions derived from the millimeter-interferometer data are listed (see §4.1), which have an accuracy of  $\sim 1''$ . Only for L1535 IRS and L1527 IRS do these positions differ by 4''–5'' from the values listed by TGWW.

Upper limits to the mass of the central stars can be obtained by assuming that all bolometric luminosity is stellar and that the object is located on the birthline in the Hertzsprung–Russell diagram (Stahler 1988; Palla & Stahler 1993). The inferred maximum masses range between 0.15  $M_{\odot}$  for TMC 1 and 2.6–2.7  $M_{\odot}$  for L1551 IRS 5 and T Tau, and are listed in Table 1. For T Tau N and S masses of 2 and 1  $M_{\odot}$ , respectively, are inferred by Bertout (1983) and Beckwith et al. (1990). Leinert & Haas (1989) quote a mass of 1.0–1.5  $M_{\odot}$  for Haro 6–10. Both of these objects are located close to the birthline, and the inferred values from Table 1 are near their true masses.

As part of the TGWW sample, our sources have been studied previously by various authors. Moriarty-Schieven et al. (1992, 1994, 1995) observed the sample in single-dish continuum emission

at 800  $\mu\text{m}$  and 1.1 mm, and in transitions of CO, CS and H<sub>2</sub>CO, deriving envelope masses and beam-averaged densities. We will use their 1.1 mm fluxes in our analysis. Kenyon et al. (1993a, 1993b) modeled the spectral energy distributions (SEDs) of an overlapping sample of YSOs, and observed and modeled the near-infrared emission. They found that the SEDs and the near-infrared images can be reproduced by the collapse model of Terebey et al. (1984), but that a cleared-out bipolar cavity is required in many cases to simultaneously fit the near-infrared and far-infrared emission. Ohashi et al. (1991, 1996) performed interferometric observations of CS 2–1 of seven objects of our sample, as well as of some more evolved T Tauri objects.

### 3. Observations

An overview of the data obtained for each source is given in Table 3. In the following the details of the observations are discussed.

#### 3.1. Interferometer observations of millimeter-continuum emission

Observations of the continuum emission at 3.4 mm and 2.7 mm were obtained with the Owens Valley Radio Observatory (OVRO) Millimeter Array<sup>1</sup> between 1992 and 1997, simultaneously with the HCO<sup>+</sup> 1–0, and the <sup>13</sup>CO and C<sup>18</sup>O 1–0 transitions, respectively. During the 3.4 mm observations the array consisted of five antennas; the 2.7 mm observations were made with a six-element array. Two sources were observed per track. Data taken in the low-resolution and equatorial configurations were combined, resulting in a  $uv$  coverage with spacings between 4 and 40 k $\lambda$  at 3.4 mm and between 4 and 80 k $\lambda$  at 2.7 mm. This corresponds to naturally weighted, synthesized beams of 6'' and 3'' FWHM, respectively. The observations of T Tau were made in five different array configurations (van Langevelde, van Dishoeck & Blake 1994a). The lower and upper-sideband continuum signals were recorded separately over the full instantaneous 1 GHz IF-bandwidth. The data were calibrated using the MMA package, developed specifically for OVRO (Scoville et al. 1993). The quasars PKS 0333+321 and 0528+134 served as phase calibrators (0420–014 for the observations of T Tau); the amplitudes were calibrated on 3C 454.3 and 3C 273, whose fluxes at the time were determined from observations of the planets.

The interferometer data were edited in the usual manner by flagging data points with clearly deviating amplitudes and phases. Editing was especially necessary for day-time observations at 2.7 mm, when the phase stability of the atmosphere can be low. The final  $1\sigma$  RMS noise value of the visibilities is approximately 4 mJy when vector averaged over 10 k $\lambda$  wide  $uv$  intervals (see §4.1). The naturally weighted, cleaned images have a typical  $1\sigma$  noise level of 2 mJy  $\text{bm}^{-1}$ .

---

<sup>1</sup>The Owens Valley Millimeter Array is operated by the California Institute of Technology under funding from the U.S. National Science Foundation (#AST93–14079).

Reduction and analysis of the visibility data was carried out within the MIRIAD software package.

### 3.2. Single-dish observations of $\text{HCO}^+$ and $\text{H}^{13}\text{CO}^+$ emission

Maps of  $\text{HCO}^+$   $J = 1-0$  (89.18852 GHz) emission were obtained with the IRAM 30m telescope, covering regions between  $112'' \times 112''$  and  $168'' \times 168''$  (approximately 16,000–24,000 AU in diameter; see Fig. 4). The maps were sampled at intervals between  $12''$  and  $28''$  depending on the source, with a beam size of  $28''$ . The data were obtained in position-switched mode, with a typical switch of  $15'-30'$  in right ascension. Special care was taken to ensure that the off positions were free of  $\text{HCO}^+$  emission. Pointing was checked regularly, and the maps were obtained in such a way as to minimize systematic effects of pointing drifts. The remaining pointing error is smaller than  $5''$ . The spectra were obtained at a frequency resolution of 40 kHz ( $0.14 \text{ km s}^{-1}$ ), and were converted to the main-beam temperature scale using  $\eta_{\text{mb}} = 0.60$ , resulting in an RMS noise level of typically 0.4 K per channel. For T Tau a region of  $30'' \times 30''$  was mapped with a grid spacing of  $15''$ , and a RMS noise level of 0.16 K at a velocity resolution of  $0.33 \text{ km s}^{-1}$ .

In the  $\text{HCO}^+$   $J = 3-2$  (267.55762 GHz) and  $4-3$  (356.73429 GHz) transitions the sources were mapped over a  $40'' \times 40''$  ( $5600 \times 5600$  AU) region at the James Clerk Maxwell Telescope<sup>2</sup>(JCMT). The maps were sampled at  $5''-10''$  intervals, corresponding to  $\frac{1}{2}-\frac{2}{3}$  times the beam sizes of  $19''$  (267 GHz) and  $14''$  (356 GHz), respectively. The observations were obtained in position-switched mode, with a typical switch of  $15'-30'$  in right ascension, again to ensure that the spectra are not contaminated by  $\text{HCO}^+$  emission at the off position. Pointing was checked regularly, and the remaining uncertainty is less than  $5''$ . The spectra were recorded with the Digital Autocorrelation Spectrometer (DAS) backend with a typical resolution of 156 kHz ( $0.15-0.18 \text{ km s}^{-1}$ ). Since the local oscillator of the 267 GHz receiver at the JCMT has no phase-lock loop, the  $\text{HCO}^+$   $3-2$  spectra have a minimum effective line width of  $\sim 0.5-1.0 \text{ km s}^{-1}$ . The spectra have been converted to the main-beam antenna temperature scale using  $\eta_{\text{mb}} = 0.69$  (267 GHz) and  $\eta_{\text{mb}} = 0.58$  (356 GHz), obtained from measurements of Jupiter and Mars by the JCMT staff. Typical resulting RMS noise levels are 0.2–0.4 K per channel on the main-beam temperature scale.

Observations of  $\text{HCO}^+$   $3-2$  toward all 24 sources of TGWW were obtained with the JCMT in 1993 August. During these observations the effective calibration was ill determined because of technical difficulties. From comparison with spectra obtained in 1995, main beam efficiencies between  $\eta_{\text{mb}} = 0.69$  and 0.31 were obtained, resulting in a calibration uncertainty of at least 30%.

Observations of  $\text{H}^{13}\text{CO}^+$   $3-2$  (260.25548 GHz) and  $4-3$  (346.99854 GHz) were also obtained at the JCMT toward the source positions. Instead of a position switch, a beam switch of  $180''$  was

---

<sup>2</sup>The James Clerk Maxwell Telescope is operated by the Joint Astronomy Centre, on behalf of the Particle Physics and Astronomy Research Council of the United Kingdom, the Netherlands Organization for Scientific Research, and the National Research Council of Canada.

used in 1996 May. Typical RMS noise levels are 60–100 mK on the main-beam temperature scale at  $0.14 \text{ km s}^{-1}$  resolution. Nobeyama 45m telescope maps in  $\text{H}^{13}\text{CO}^+$  1–0 of five of our sources have been presented by Mizuno et al. (1994). The single-dish observations were further reduced and analyzed with the CLASS software package.

## 4. Disk and envelope continuum emission

### 4.1. Millimeter-continuum visibilities

In order to study the evolution of the circumstellar disks and envelopes around YSOs, it is necessary to accurately separate their respective contributions to the millimeter-continuum emission. For this purpose, the interferometer observations are best represented in the  $uv$  plane. Since visibilities are complex quantities, only combinations of the real and imaginary parts can be plotted. The vector average of the amplitudes with respect to a given phase center corresponds to the Fourier transform of those components of the sky-brightness distribution which are symmetric around that position. It is important to use the correct source position as the phase center, because an offset of the order of the synthesized beam ( $3''$ – $6''$ ) or more creates an artificial decrease of flux with  $uv$  distance. Since amplitudes are never negative, random noise in the complex visibilities translates to a non-zero expectation value for the vector-averages even in the absence of emission.

In Fig. 2 the vector-averaged and  $uv$ -binned visibilities of our sources are shown as functions of  $uv$  distance, with their  $1\sigma$  error bars and zero-signal expectation values. The positions of the unresolved point sources were adopted as phase centers (see below and Table 1). As a reference, the naturally weighted, cleaned images are also presented. All nine sources are detected in 3.4 and 2.7 mm continuum emission, with total fluxes ranging between 4 and 200 mJy. Three sources, L1489 IRS, L1535 IRS and TMC 1, are detected above the zero-signal expectation value in only one or two  $uv$  bins. However, the continuum positions listed in Table 1 agree well with the  $2 \mu\text{m}$  positions, and the objects can be clearly discerned in the cleaned images. It is therefore concluded that these are true detections. The other six sources are confidently detected above the noise level in all  $uv$  bins.

Because the vector-averaged fluxes form the Fourier transform of the sky brightness, the signal of a point source is constant with  $uv$  distance in the absence of noise, while that of an extended structure is a decreasing function of  $uv$  separation. Emission on scales larger than  $\sim 50''$  (corresponding to the shortest spacing of  $\sim 4 \text{ k}\lambda$ ) is resolved out altogether by the array; on intermediate scales only part of the flux is recovered, depending on the  $uv$  coverage. Such resolved emission is detected on top of unresolved emission toward five sources: T Tau, Haro 6–10, L1551 IRS 5, TMR 1 and L1527 IRS. The uncertain  $uv$  dependence of the visibilities of the weaker sources L1489 IRS, L1535 IRS, and TMC 1 precludes any statement about the spatial distribution of their continuum emission.



The observed visibilities, and not just their vector averages, were fit with a source model consisting of a point source plus an extended Gaussian component whenever necessary. This method has been applied previously to the millimeter-continuum emission of YSOs by, e.g., Keene & Masson (1990), Terebey et al. (1993), and Butner et al. (1994). These authors, however, use a complete envelope model to describe the extended component. Because of the limited signal-to-noise ratio and  $uv$  coverage of our data, such level of detail is unwarranted. The obtained fit parameters (position, point-source flux, flux and FWHM of the extended component) are listed in Table 4. The unresolved point sources have sizes  $< 3''$  ( $< 420$  AU in diameter). Their positions are listed in Table 1 and agree within  $2''$  with the near-infrared positions, except for L1527 IRS and L1535 IRS, which are shifted by  $\sim 5''$  to the northeast and north, respectively. Ladd et al. (1991) and Fuller et al. (1996) found a similar shift for L1527 IRS from single-dish millimeter continuum maps. In the following, only the point-source fluxes will be used quantitatively in the analysis; the inferred values for the extended sources are not sufficiently reliable for further interpretation.

Of the sources in our sample only Haro 6–10 had not been observed previously by millimeter interferometry; all others have been observed before, though generally at a lower signal-to-noise ratio, resulting in fewer detections. The total 2.7 mm flux levels range between 4 mJy and 200 mJy, and agree well with those listed by Keene & Masson (1990), Ohashi et al. (1991, 1996) and Terebey et al. (1993). At the position of the reported companion of L1527 IRS (Fuller et al. 1996) no continuum emission is detected at 2.7 mm at an estimated  $1\sigma$  noise level of  $4 \text{ mJy bm}^{-1}$ , taking into account primary beam attenuation and  $uv$  coverage.

The unresolved point-source emission seen by millimeter interferometers around YSOs is usually attributed to thermal emission from an optically thick circumstellar disk (e.g., Terebey et al. 1993). Lay et al. (1994) and Mundy et al. (1996) have resolved the circumstellar disks around HL Tau and L1551 IRS 5 with the JCMT–CSO single-baseline and BIMA interferometers. They find sizes of 60–80 AU for the semi-major axes of these disks, consistent with the upper limits found here. Spectral indices over  $\lambda = 2.7 \text{ mm}$  to  $870 \mu\text{m}$  of  $\alpha = 2.7$  and 2.5, respectively, are inferred. The recent identification of L1551 IRS 5 as a binary system instead of a resolved disk (Looney et al. 1997) does not influence the inferred value for  $\alpha$ . Van Langevelde et al. (1995) find  $\alpha \approx 2.5$  between 2.7 mm and  $840 \mu\text{m}$  for T Tau, although possible variability and decomposition into thermal and non-thermal contributions for T Tau N and S complicate the interpretation (see also Hogerheijde et al. 1998b).

Non-thermal contribution to the continuum flux of YSOs at millimeter wavelengths could come from free–free emission of an ionized wind. Fluxes at 2, 3.6 and 6 cm are given for some of our sources by Rodríguez et al. (1989), Keene & Masson (1990) and Skinner & Brown (1994). From these values and the expected flat free–free spectrum, it is estimated that this mechanism does not provide more than 10% of the 2.7 mm flux of the YSOs observed here (cf. Keene & Masson 1990; Lay et al. 1994). Only for T Tau may up to 30% of the 2.7 mm flux be attributed to free–free emission (Skinner & Brown 1994; van Langevelde et al. 1995; Hogerheijde et al. 1998b).

The millimeter-continuum visibilities show that at least two-thirds of the embedded sources selected here are surrounded by compact disks. This detection rate is significantly larger than that of 15% reported by Ohashi et al. (1996) for a largely identical sample, owing entirely to the differences in sensitivity ( $2 \text{ mJy bm}^{-1}$  vs.  $3\text{--}7 \text{ mJy bm}^{-1}$ ). The inferred 2.7 mm disk fluxes range between 7 and 100 mJy, which may correspond to ranges in disk size, density, temperature, orientation, or mass. It is therefore not straightforward on the basis of these fluxes alone to investigate evolutionary effects, such as disk growth. Comparison with point source fluxes of more evolved class II objects is further complicated by the fact that this phase lasts ten times longer than the embedded phase. During this evolutionary period significant dispersal of the disk is expected, and it is not clear which objects represent the youngest class II sources (cf. Ohashi et al. 1996). Dutrey et al. (1996) find an average flux at 2.7 mm of  $\sim 24 \text{ mJy}$  for a sample of 12 T Tauri stars with the Plateau de Bure Interferometer, comparable to the flux levels found toward our embedded sources.

#### 4.2. Separating envelope and disk flux at $\lambda = 1.1 \text{ mm}$

Moriarty-Schieven et al. (1994) obtained the continuum flux at 1.1 mm of the TGWW sample in a  $19''$  beam with the JCMT. The flux of Haro 6–10 is given by Kenyon et al. (1993a). These single-dish measurements contain contributions from the extended envelope as well as any compact disk. The point-source fluxes derived in the previous section can be used to separate these components if a spectral index for the point-source emission between  $3.4/2.7 \text{ mm}$  and  $1.1 \text{ mm}$  is known or adopted. Since all our sources have good signal-to-noise single-dish fluxes, reliable envelope fluxes can be obtained even for those sources which have only marginal detections in the interferometer beam.

For typical densities and values of the dust emissivity, the envelope is optically thin at  $1.1 \text{ mm}$ , and its flux traces all the mass within the beam. The unresolved circumstellar disks, on the contrary, are likely to be optically thick. For a sharp-edged, isothermal, unresolved disk and optically thick emission, a spectral slope of  $\alpha = 2.0$  is expected. More realistic disks, with radial surface-density and temperature gradients, may have  $\alpha > 2$ , because the optically thick area increases for shorter wavelengths. A maximum value for  $\alpha$  is found from the ratio of the  $3.4/2.7 \text{ mm}$  OVRO and  $1.1 \text{ mm}$  JCMT fluxes, and ranges between 2.4 and 4.0. These are strict upper limits since extended emission is actually observed toward half of the sources in the interferometer beam. In the following,  $\alpha = 2.5$  will be assumed as a best estimate for the spectral slope of the disk based on the measured values for HL Tau, L1551 IRS 5, and T Tau. The effect of over- or underestimating  $\alpha$  is to attribute too little, or too much, respectively, of the  $1.1 \text{ mm}$  flux to the envelope. Sources with relatively weak fluxes at  $1.1 \text{ mm}$  are worst affected by the uncertainty in  $\alpha$ . However, none of the results from the subsequent analysis depend critically on the assumed value.

In Table 5 the  $1.1 \text{ mm}$  single dish fluxes from Moriarty-Schieven et al. (1994) and the

estimated envelope contributions are listed. The envelopes and disks are found to contribute equally to the single-dish fluxes: approximately 30–75% of the single-dish flux at 1 mm originates in the envelope; for  $\alpha = 2.0$  this would be 50–85%. Toward Haro 6–10 all single-dish flux can be attributed to the point source detected at 2.7 mm, although an extended component appears also present in the visibilities (see Fig. 2). No constraints on the spatial distribution of the 3.4 and 2.7 mm emission were obtained in §4.1 for L1489 IRS, L1535 IRS and TMC 1, resulting in a range of possible envelope fluxes. These caveats are included in the estimated error bars on the fluxes in the analysis below.

### 4.3. Mass estimates for the envelopes and disks

The envelope mass traced in the 19'' JCMT beam can be obtained, assuming optically thin emission from the relation

$$M = \frac{F_\nu D^2}{\kappa_\nu B_\nu(T_d)} \left( \frac{\tau_\nu}{1 - e^{-\tau_\nu}} \right), \quad (1)$$

where  $M$  is the mass,  $F_\nu$  is the 1.1 mm (envelope) flux,  $D$  is the distance to Taurus (140 pc),  $\kappa_\nu$  is the dust emissivity at 1.1 mm per unit total mass, and  $B_\nu(T_d)$  is the Planck function at the dust temperature  $T_d$ . For  $\kappa_\nu$  a value of  $0.01 \text{ cm}^2 \text{ g}^{-1}$  is adopted (Agladze et al. 1994; Pollack et al. 1994; Ossenkopf & Henning 1994). A dust temperature  $T_d = 30 \text{ K}$  is assumed, consistent with the average temperature inferred from SED fitting by Moriarty-Schieven et al. (1994). The obtained envelope masses range from  $< 0.0014 M_\odot$  for Haro 6–10 to  $0.26 M_\odot$  for L1551 IRS 5, and are listed in Table 5.

Using the same expression, a lower limit to the mass of the disks can be obtained, again assuming  $\tau_\nu \ll 1$ . Since the disks are likely to be optically thick at 3.4/2.7 mm, only lower limits are found. Using the same dust emissivity of  $0.01 \text{ cm}^2 \text{ g}^{-1}$  scaled by  $(\lambda/1.1 \text{ mm})^{-1.5}$  and a dust temperature of 30 K, disk masses between  $4 \times 10^{-3} M_\odot$  for L1489 IRS and  $7 \times 10^{-2} M_\odot$  for L1551 IRS 5 are inferred (see Table 4), i.e., a factor of  $\sim 3$  less than the envelope masses. For a higher dust temperature the inferred disk masses decrease as  $M \propto T_d^{-1}$ , while for significant optical depth they increase as  $M \propto \tau_\nu$  for  $\tau \gg 1$ . Given the fact that the disks likely have  $\tau_\nu \gtrsim 1$ , it is concluded that the disks and envelopes typically are equally massive, with each carrying  $\sim 10\%$  of the mass of the central object (cf. Table 1).

## 5. HCO<sup>+</sup> and H<sup>13</sup>CO<sup>+</sup> emission

In Fig. 3 the HCO<sup>+</sup> 1–0, 3–2 and 4–3, and H<sup>13</sup>CO<sup>+</sup> 3–2 and 4–3 spectra obtained toward the source positions are presented. In Fig. 4 contour maps of the emission integrated over the full width of the HCO<sup>+</sup> lines are shown. The 50% intensity contours are indicated by the thick solid lines in all maps. The observed velocity-integrated intensities toward the source centers and the

FWHM of the maps are listed in Table 6.

Toward the majority of sources the  $\text{HCO}^+$  spectra are dominated by a relatively narrow line ( $\Delta V \approx 2\text{--}3 \text{ km s}^{-1}$ ). Double-peaked line profiles are present toward most sources. Since care was taken to obtain emission-free reference positions (§3.2), these can be attributed to self-absorption. Red-shifted self-absorption features in a high-excitation line like  $\text{HCO}^+$  4–3 are sometimes invoked as a tracer of protostellar infall (Walker et al. 1986; Zhou et al. 1993; Zhou 1995; Ward-Thompson et al. 1996). It should be noted that such features are only prominently present toward two of our sources, L1489 IRS and L1527 IRS. The occurrence of blue-shifted absorption, or the absence of any features altogether, indicates that other factors like orientation are equally important in determining the shape of the line profiles. For example, toward T Tau the absorption seen in interferometer data is filled in by emission from the surrounding cloud in the single-dish observations (van Langevelde et al. 1994a).

In many spectra, emission from the bipolar outflow is visible as line wings, but only toward T Tau do the wings dominate the total intensity. The integrated intensities listed in Table 6 and the contour maps shown in Fig. 4 therefore predominantly reflect the quiescent envelope material. For T Tau, estimates of the relative contributions of the envelope and the outflow are given in the table. The  $\text{H}^{13}\text{CO}^+$  lines are narrow, with  $\Delta V = 0.5\text{--}3.0 \text{ km s}^{-1}$ , peaking at the same velocity as the  $\text{HCO}^+$  absorption features, if present.

The average optical depth  $\bar{\tau}$  over the  $\text{HCO}^+$  line profiles can be estimated from the ratio of the  $\text{HCO}^+$  and  $\text{H}^{13}\text{CO}^+$  integrated intensities, assuming an abundance ratio of 65:1 for  $[\text{HCO}^+]:[\text{H}^{13}\text{CO}^+]$ . Typical opacities of 4–10 or less are found (see Table 6). Larger optical depths are inferred for the 1–0 lines of L1527 IRS and TMC 1A, with  $\bar{\tau} \approx 18\text{--}21$ . The  $\text{H}^{13}\text{CO}^+$  lines are optically thin in all observed transitions and toward all sources.

A beam-averaged  $\text{HCO}^+$  abundance can be obtained from the  $\text{H}^{13}\text{CO}^+$  1–0 intensities toward L1551 IRS 5, L1535 IRS, TMR 1, and L1527 IRS (Mizuno et al. 1994), and the  $\text{C}^{18}\text{O}$  1–0 data of Hayashi et al. (1994), in respective beams of  $19''$  and  $15''$ . Assuming LTE at an excitation temperature  $T_{\text{ex}}$ , the beam-averaged column density in  $\text{cm}^{-2}$  is given in cgs units by

$$\bar{N} = 10^5 \times \frac{3k^2}{4h\pi^3\mu^2\nu^2} \exp\left(\frac{h\nu J_l}{2kT_{\text{ex}}}\right) \frac{T_{\text{ex}} + h\nu / 6k(J_l + 1)}{e^{-h\nu/kT_{\text{ex}}}} \int T_{\text{mb}} \left( \frac{\tau}{1 - e^{-\tau}} \right) dV \quad (2)$$

(Scoville et al. 1986), where  $\int T_{\text{mb}} dV$  is the integrated intensity in  $\text{K km s}^{-1}$  of the  $J_u\text{--}J_l$  transition with frequency  $\nu$  and opacity  $\tau$ . The permanent dipole  $\mu$  is 0.112 Debye and 3.91 Debye for  $\text{C}^{18}\text{O}$  and  $\text{H}^{13}\text{CO}^+$ , respectively (Millar et al. 1991). With critical densities of  $2 \times 10^5 \text{ cm}^{-3}$  and  $2 \times 10^3 \text{ cm}^{-3}$ , respectively, the excitation of  $\text{H}^{13}\text{CO}^+$  1–0 and  $\text{C}^{18}\text{O}$  1–0 is likely to be thermalized, especially in the inner dense regions of the envelope. Assuming the same abundance ratio for  $[\text{HCO}^+]:[\text{H}^{13}\text{CO}^+]$  of 65:1, a ratio of  $[\text{H}_2]:[\text{C}^{18}\text{O}]$  of  $5 \times 10^6$ , and an excitation temperature of 30 K, an abundance of  $\text{HCO}^+$  of  $(1.2 \pm 0.4) \times 10^{-8}$  is found. The uncertainty in this value is dominated by the spread in the data points of the five sources. This value is comparable to that inferred for dark clouds of  $\sim 8 \times 10^{-9}$  (Irvine et al. 1987), and it is assumed that it can be applied

to all sources in our sample.

In the maps of integrated  $\text{HCO}^+$  1–0 intensity, each source shows up as a distinct core of roughly  $50''$ – $150''$  in diameter ( $28''$  beam size), superposed on extended emission from the surrounding cloud. The enhancement in integrated intensity around the sources arises partially from the increased line widths. At positions  $\sim 60''$  (8400 AU) away from the center, the average  $\text{HCO}^+$  1–0 line width has decreased from  $2.0$ – $3.0 \text{ km s}^{-1}$  to  $0.5$ – $1.0 \text{ km s}^{-1}$ . The emission in  $\text{HCO}^+$  3–2 and 4–3 is much more concentrated around the sources, with typical sizes of  $20''$ – $30''$  in diameter compared with the respective beam sizes of  $19''$  and  $14''$ . The 50% intensity contours are nearly circular and all cores appear marginally resolved with FWHM  $\sim 1.5$  times the beam size. This is typical for density distributions following a radial power law, i.e., distributions without an intrinsic size scale within the sampled range. This point is illustrated by Ladd et al. (1991) and Terebey et al. (1993) for continuum emission; line emission does possess an intrinsic density scale. The  $\text{HCO}^+$  3–2 and 4–3 emission around T Tau shows a prominent extension toward the southwest, which is also seen in several transitions of CO (Edwards & Snell 1982; Schuster et al. 1993) and is probably associated with the reflection nebula NGC 1555.

For the scope of this paper, i.e., the comparison of the continuum flux with the  $\text{HCO}^+$  line emission as tracers of the circumstellar envelopes, the spherically averaged quantities listed in Table 6 suffice. In a future paper (Hogerheijde et al. 1998c), the line profiles will be studied in greater detail.

## 6. Analysis

The observed integrated  $\text{HCO}^+$  3–2 and 4–3 intensities are compared with the 1.1 mm envelope fluxes in Fig. 5, and are seen to correlate well. Since the  $\text{HCO}^+$  line intensities depend primarily on density and mass, whereas the continuum fluxes scale with dust temperature and mass, the apparent correlation suggests that both quantities primarily trace envelope mass.

The inferred envelope continuum fluxes at 1.1 mm and the  $\text{HCO}^+$  observations presented above allow further investigation into the mass and density structure of the circumstellar material around the objects of our sample. From the beam-convolved  $\text{HCO}^+$  source sizes it was concluded that the envelopes do not possess any intrinsic scale within the sampled range, i.e., their density follows a radial power law. Many models of protostellar collapse predict such a density distribution. The precise value of the power-law index and its evolution with time depend on the formulation of the problem and distinguish the various proposed models (e.g., Shu 1977, Terebey, Shu & Cassen 1984, Galli & Shu 1993, Fiedler & Mouschovias 1992, 1993, Boss 1993, and Foster & Chevalier 1993). In this section the envelope fluxes and integrated  $\text{HCO}^+$  intensities will be compared with one such model, namely the self-similar, inside-out collapse model of Shu (1977). Although this model is obviously oversimplified, it has the advantage that it depends on only two parameters: the sound speed  $a$ , and the initial mass of the cloud core, or, equivalently, its initial

outer radius  $R$ . Since the objects in our sample are all located within the similar environment of a single star-forming region, the dependence on these parameters is minimized. Because of the simple formulation of this model, it has been used widely for comparison to observations (Zhou 1992; Zhou et al. 1993; Choi et al. 1995; Ceccarelli et al. 1996). Formally, the assumption of self-similarity breaks down when the so-called collapse expansion wave reaches the outer radius. However, we will continue to use this formulation even after this time as a qualitative description.

### 6.1. Parameters of the model calculations

The inside-out collapse model has only two main parameters: the sound speed  $a$  and the initial core radius  $R$ . In addition, the dust emissivity  $\kappa_\nu$  at 1.1 mm (§4.3), the  $\text{HCO}^+$  abundance (§5), and the temperature of the gas and the dust are required to calculate the emergent continuum flux and  $\text{HCO}^+$  line strengths. The density configuration of the initial state is given by  $\rho(r) = (a^2/2\pi G)r^{-2}$ , and its mass by  $M(R) = 2Ra^2/G$ . Estimates for the sound speed in the Taurus cloud cores vary between  $a = 0.2$  and  $0.43 \text{ km s}^{-1}$  (Terebey et al. 1984). A value of  $a = 0.3 \text{ km s}^{-1}$  is used here, corresponding to the isothermal sound speed for the typical temperatures of  $\sim 30\text{--}40 \text{ K}$  derived by Moriarty-Schieven et al. (1994). In addition, it is the smallest value which can explain the observed 1.1 mm continuum flux of L1551 IRS 5 ( $\sim 3 \text{ Jy}$ ). It should be noted that the density, flux and mass are strongly dependent on  $a$ , with  $\rho \propto a^2$  and  $M \propto a^3$ .

Estimates for the core radius can be obtained from the  $\text{HCO}^+$  1–0 and 3–2 maps, and from the  $\text{C}^{18}\text{O}$  2–1 emission observed at positions more than  $30''\text{--}60''$  away from the source centers (Hogerheijde et al. 1998a). The density at these positions has dropped to  $(0.3\text{--}3.0)\times 10^4 \text{ cm}^{-3}$ , representative of the surrounding cloud. With  $a = 0.3 \text{ km s}^{-1}$ , this corresponds to a radius of  $R = 9000\text{--}28,000 \text{ AU}$  where the core merges into the surrounding cloud. Since most of the continuum and line emission originates from the central regions of the core, especially for the  $\text{HCO}^+$  3–2 and 4–3 lines which possess critical densities  $\geq 10^6 \text{ cm}^{-3}$ ,  $R = 9000 \text{ AU}$  ( $65''$ ) will be used. Another estimate of the core size can be obtained from the observed line widths in the surrounding cloud, typically  $\Delta V \approx 0.4 \text{ km s}^{-1}$ . A turnover radius can be defined where the kinetic energy contained in these motions,  $\sim \frac{1}{2}(\Delta V)^2$ , balances the gravitational binding to a  $M_\star \approx 0.5 M_\odot$  object,  $GM_\star/R$ . From such an analysis, a value of  $R \approx 10,000 \text{ AU}$  is found, in good agreement with the adopted  $R = 9000 \text{ AU}$ .

The total envelope mass depends strongly on  $R$ , with  $M_{\text{env}} \propto R$ , and is therefore not well constrained by the observations. For  $R = 9000 \text{ AU}$ ,  $M_{\text{env}} = 1.8 M_\odot$  is obtained, a factor of 3 higher than the average stellar mass in Taurus. However, the bipolar outflow may disperse part of the envelope, or even reverse infall before all envelope mass has accreted onto the protostar. The mass-accretion rate corresponding to  $a = 0.3 \text{ km s}^{-1}$  is  $\dot{M}_{\text{acc}} = 6 \times 10^{-6} M_\odot \text{ yr}^{-1}$ . If the accretion rate onto the star is the same as this large scale envelope accretion rate, a luminosity of  $L_{\text{acc}} = GM_\star\dot{M}_{\text{acc}}/R_\star = 32 L_\odot$  is generated, assuming a stellar mass of  $0.5 M_\odot$  and radius of

$3 R_{\odot}$ . This accretion luminosity is much larger than the typical observed values for our sources, but a non-constant accretion rate onto the star can result in a significantly reduced luminosity during large periods of time separated by short outbursts of high luminosity (cf. FU Orionis events; see Hartmann, Kenyon & Hartigan 1993, and §6).

The inside-out collapse model is based on isothermal initial conditions. After the onset of collapse and the formation of a central object, this assumption no longer holds. A simple power-law behavior for the dust temperature distribution is assumed,  $T_d \propto r^{-0.4}$ , as is valid for any centrally heated envelope which is optically thin to the photons carrying the bulk of the heating (e.g., Rowan-Robinson 1980). At a characteristic radius of 1000 AU,  $T_d = 30$  K is assumed, consistent with recent calculations of the dust temperature distribution in YSO envelopes (e.g., Ceccarelli et al. 1996). Although the gas and the dust are not closely coupled thermally at the lower densities, the simplifying assumption  $T_{\text{kin}} = T_d$  is made for all radii. Recent calculations by Ceccarelli et al. (1996) indicate that the gas kinetic temperature does not deviate from the dust temperature by more than a factor of  $\sim 2$ .

For comparison, calculations are also made for power-law density distributions,  $\rho(r) = \rho_0 (r/r_0)^{-p}$ , with  $p = 1, 2$  and  $3$ . The same outer radius  $R$ , dust emissivity,  $\text{HCO}^+$  abundance and temperature structure as for the collapse model are used.

## 6.2. Comparison of model calculations with observations

Since the continuum emission at 1.1 mm is optically thin, the flux as observed in a  $19''$  beam can be easily calculated as a function of time by direct integration along all lines of sight. The results are shown in Fig. 6a. It should be stressed that the time-axis has no quantitative meaning, since the mass-accretion rate, and hence the mass of the envelope as function of time, is strongly dependent on the ill-constrained sound speed. Furthermore, the evolution is followed beyond the point where the assumption of self-similarity breaks down, as indicated by the vertical dashed line, in that the envelope fluxes observed toward almost the entire source sample fall beyond this line. The results are therefore more realistically presented as a function of density at the arbitrary radius of 1000 AU. This approach is used in Fig. 6b, which presents curves for the collapse and three power-law models.

In Table 5 the  $\text{H}_2$  number densities at 1000 AU corresponding to the inferred envelope fluxes are listed for the collapse model curve; values range between  $1 \times 10^4$  and  $2 \times 10^6 \text{ cm}^{-3}$ , and depend on the adopted dust temperature. Since the disks are estimated to contribute 30–75% to the total 1.1 mm flux, the inferred densities do not depend critically on the assumed value for the spectral index  $\alpha$ . For Haro 6–10, where all single-dish flux can be attributed to a disk, only an upper limit to the density is found.

To calculate the  $\text{HCO}^+$  emission of the model envelopes, the excitation must to be solved together with the radiative transfer, since the lines are generally optically thick. A one-dimensional

Monte Carlo code has been used, based on the description of Bernes (1979). The radiation field at all transition frequencies is represented simultaneously by 200 model photons propagating through the model envelope. The  $\text{HCO}^+\text{-H}_2$  collision rates of Monteiro (1985) and Green (1975) have been used, together with the line frequencies of Blake et al. (1987). The model is divided into 15 concentric shells, each with a density following the inside-out collapse model or any of the three power-law descriptions, a kinetic temperature, and fractional abundances for  $\text{HCO}^+$  and  $\text{H}^{13}\text{CO}^+$ . No abundance variations with radius have been adopted. Instead of a detailed velocity field, a turbulent line width of  $1.0 \text{ km s}^{-1}$  FWHM has been used throughout the model envelope. This produces line widths comparable to the observed spectra. For the excitation of lines for which the envelope is transparent (e.g.,  $\text{H}^{13}\text{CO}^+$ ), the details of the velocity field are not important. Significant optical depths are obtained for  $\text{HCO}^+$ , but it is found that the resulting integrated line intensities do not depend strongly on the details of the velocity field, and stay well within the estimated uncertainty of a factor of  $\sim 2$  originating from the other parameters of the source model, i.e., sound speed, temperature, and abundance. After the molecular excitation has converged, the radiative transfer is solved. The resulting sky-brightness distribution is then convolved with the appropriate beam sizes.

Line intensities and FWHM source sizes predicted by the Monte Carlo code are shown in Fig. 6c and 6d as functions of density for the four models. The behavior of the curves reflects the increasing molecular column density with larger  $n_{\text{H}_2}$ , resulting in higher line intensities and larger source sizes. At high column density, the intensities level off because of optical depth. Since the curves are parameterized by the density at 1000 AU, the central density is lower for the  $p = 1$  model than for the  $p = 3$  model at the same  $n_{\text{H}_2}$ . This explains why the model curves can cross. The behavior of the collapse-model curve is best understood in terms of time, indicated along the top of the panels, rather than density. For example the decrease of the  $\text{HCO}^+$  line intensities with time of  $20\text{--}30 \text{ K km s}^{-1}$  to a few  $\text{K km s}^{-1}$  between  $t \sim 10^4 \text{ yr}$  and a few  $\times 10^6 \text{ yr}$  reflects the decreasing density and column density of the envelope. The  $\text{H}^{13}\text{CO}^+$  1–0, 3–2 and 4–3 line intensities decrease from  $10\text{--}15 \text{ K km s}^{-1}$  to  $< 0.2 \text{ K km s}^{-1}$  over the same time span. Lower bounds to the observational sensitivities are typically  $0.2\text{--}0.7 \text{ K km s}^{-1}$ , so that the data can probe the full parameter range. The FWHM sizes of the beam-convolved model  $\text{HCO}^+$  emission vary from  $70''\text{--}110''$  (1–0),  $30''\text{--}110''$  (3–2), and  $20''\text{--}60''$  (4–3). The maximum in the convolved source size around  $t \sim 10^5 \text{ yr}$  corresponds to the moment when the collapse expansion wave reaches the outer radius of the envelope, and the density follows  $\rho \propto r^{-1}$  over a large region. A flatter density distribution results in a more extended sky-brightness distribution, and hence a larger convolved source size. The time variation of the column density and the steepening of the density distribution drive the evolution of the integrated intensities and FWHM source sizes. The small observed source sizes in 3–2 and 4–3 exclude density distribution as flat as  $p < 1$ . Otherwise, no strong constraints are placed on the model parameters by the source sizes.

To investigate how well the different models can describe the envelopes of our sources, the calculated  $\text{HCO}^+$  intensities are plotted against the corresponding envelope fluxes in Fig. 5. The



individual sources are identified in the  $\text{HCO}^+$  3–2 panel. Whereas the continuum flux only traces mass, the  $\text{HCO}^+$  lines probe both density and mass. For the inside-out collapse model, time runs from the upper-right to lower-left corners of the panels; the density at 1000 AU decreases in that same direction for all four curves. The observations are plotted with error bars corresponding to the  $\sim 20\%$  calibration uncertainty. For T Tau, the relatively large contribution made by the outflow to the  $\text{HCO}^+$  4–3 line wings is incorporated in the error bar. Overall, the model curves are seen to describe the observations well. The uncertainty in the model parameters and the scatter in the data points preclude any constraints on the density model, although the  $\text{H}^{13}\text{CO}^+$  4–3 data seem to favor a slope  $p \leq 2$ . To a large extent, the agreement between models and observations reflects the unsurprising fact that less massive envelopes are weaker in both continuum and line emission. However, the correlation between the envelope flux and the  $\text{HCO}^+$  intensity indicates that the observed range in either of these quantities is not due to variations in the temperature of the bulk of the dust or of the  $\text{HCO}^+$  abundance. This means that within the  $\sim 20''$  beam, no significant depletion of molecules has occurred. Only for L1551 IRS 5 do the observations fall significantly below the model curves in many of the  $\text{HCO}^+$  and  $\text{H}^{13}\text{CO}^+$  panels. One possible explanation is offered by the identification of this source as undergoing a FU Orionis outburst (cf. Mundt et al. 1985), which may result in an enhanced dust temperature and a larger continuum flux. For the sources in general, the correspondence between model curves and observations is better for the  $\text{HCO}^+$  3–2 and 4–3 lines, consistent with the maps, which show that significant contribution to the 1–0 line comes from the surrounding cloud. It is concluded that the  $\text{HCO}^+$  3–2 and 4–3 emission is a good tracer of the envelope mass.

## 7. Discussion

In the previous section it was shown that the envelopes around our nine sources, as traced by their 1.1 mm continuum emission and  $\text{HCO}^+$  3–2 and 4–3 lines, are characterized by a radial power-law density distribution with slopes  $p = 1-2$ . This is consistent with the inside-out collapse model of Shu (1977), but more detailed comparisons with line profiles should be made before further statements about the validity of any specific collapse model can be made (see Hogerheijde et al. 1998c for such an analysis of the  $\text{HCO}^+$  data presented here). Especially the  $\text{HCO}^+$  3–2 and 4–3 lines are found to be especially robust tracers of the envelopes. Similar conclusions were reached by Blake et al. (1994) for NGC 1333 IRAS 4 and van Dishoeck et al. (1995) for IRAS 16293–2422. A beam-averaged  $\text{HCO}^+$  abundance of  $(1.2 \pm 0.4) \times 10^{-8} \text{ cm}^{-3}$  is inferred from  $\text{C}^{18}\text{O}$  1–0 observations, and is found to be well-matched to the continuum fluxes, i.e., essentially undepleted abundances over  $20''$  scales. Typical masses within the  $19''$  JCMT beam of  $0.001-0.26 M_{\odot}$  are found.

Moriarty-Schieven et al. (1995) used observations of CS 3–2, 5–4 and 7–6 to investigate the envelopes around all sources from the TGWW sample. These transitions probe densities between  $10^6$  and  $10^7 \text{ cm}^{-3}$  and temperatures between 14 and 66 K, and as such should be well suited

as envelope tracers. In Fig. 7 a comparison is made between their CS data and our  $\text{HCO}^+$  3–2 measurements for the full TGWW sample. The correlation of the  $\text{HCO}^+$  3–2 (19'' beam) with the CS 3–2 line (43'' beam) and with the 5–4 line (32'' CSO beam) is found to be poor, reflecting the large contribution by the surrounding cloud to these transitions. For the 5–4 line (20'' JCMT beam) and the 7–6 line (20'' beam), essentially the same trend is observed as in  $\text{HCO}^+$  3–2, although the  $\text{HCO}^+$  3–2 is, on average, stronger by a factor of 5–10. Thus,  $\text{HCO}^+$  may be a more sensitive and easier to observe envelope tracer than CS.

Does the observed trend of  $\text{HCO}^+$  and 1.1 mm continuum flux as tracers of the envelopes also hold for the full sample defined by TGWW? In particular, are those sources which remained undetected in  $\text{HCO}^+$  3–2 also different in 1.1 mm dust continuum from the selected sources? In Fig. 8 the  $\text{HCO}^+$  3–2 observations of the full TGWW sample are plotted against their 1.1 mm fluxes from Moriarty-Schieven et al. (1994). This plot is an extension of the  $\text{HCO}^+$  3–2 panel of Fig. 5, with the only difference that no correction is made for the contribution of possible disks to the continuum flux, which is not known for the other sources. As a reference, the model curve for inside-out collapse is also shown. Note that this plot shows that the point-source subtraction is not critical for the conclusions of §6; the data points of our source sample (indicated by filled symbols) are still reasonably well fit by the model curve.

The sources which were not included in our sample are indicated by the open symbols, and can be split into two groups: those with detected, but weak  $\text{HCO}^+$  3–2 emission, and those undetected in this line. The first group forms the low-brightness tail of the  $\text{HCO}^+$ –1.1 mm-continuum distribution of our sample. These are sources with envelopes of low mass, either because they already have accreted much of their core material, or because they are intrinsically low-mass objects. The YSOs in the second group are found to span the same range in 1.1 mm flux as our subsample, and are also weak in  $\text{C}^{18}\text{O}$  3–2 (Hogerheijde et al. 1998a), indicating that the lack of  $\text{HCO}^+$  3–2 emission is due to a low total column density, and not to a low  $\text{HCO}^+$  abundance or low density. It is therefore concluded that the 1.1 mm continuum flux of these sources originates primarily in a circumstellar disk, much smaller than the 19'' JCMT beam, instead of an extended envelope. Interferometric observations of millimeter continuum toward several of these sources (DG Tau: Dutrey et al. 1996; GG Tau: Ohashi et al. 1996) are consistent with this interpretation, assuming a spectral index of  $\alpha = 2.5$ . No detectable  $\text{HCO}^+$  3–2 emission is expected from disks with such small beam-filling factors at the noise level achieved by our observations. Dutrey et al. (1997) detected an integrated  $\text{HCO}^+$  3–2 intensity of  $1.5 \text{ K km s}^{-1}$  toward GG Tau in the 9'' IRAM 30m beam, consistent with our upper limit of  $\sim 0.3 \text{ K km s}^{-1}$  in the 19'' JCMT beam for an unresolved source.

In the simple evolutionary picture sketched in §1, sources without envelopes but with disks are more evolved than those still surrounded by envelopes. Obviously, intrinsically less massive objects appear to be more evolved if judged by the absolute mass of their envelope alone. Bontemps et al. (1996) and Saraceno et al. (1996) used the envelope mass, as traced by the 1.1 mm flux, together with the bolometric luminosity to obtain an evolutionary ordering of an extended sample of YSOs.

If the mass accretion rate  $\dot{M}_{\text{acc}}$  is assumed to be constant, then the mass of the envelope at time  $t$  is given by  $M_{\text{env}} = M_0 - \dot{M}_{\text{acc}} t$ , where  $M_0$  is the initial core mass. The mass of the central object is given by  $M_{\star} = \dot{M}_{\text{acc}} t$ . The bolometric luminosity  $L_{\text{bol}}$  is a measure of  $M_{\star}$ , whether it is mainly stellar in origin, or whether it is assumed to be generated by mass accretion onto the star,  $L_{\text{bol}} = L_{\text{acc}} = GM_{\star}\dot{M}_{\text{acc}}/R_{\star}$ , with  $R_{\star}$  the radius of the protostar. In this simple scheme, the ratio of  $M_{\text{env}}$  over  $L_{\text{bol}}$  gives the relative evolutionary ‘phase’ of the object; a YSO starts off with large  $M_{\text{env}}$  and low luminosity (low  $M_{\star}$ ), and evolves toward high luminosity (large  $M_{\star}$ ) and low  $M_{\text{env}}$ . In Fig. 2 of Saraceno et al. (1996) this ratio corresponds to the relative distance traveled along the evolutionary tracks.

Based on the results of the previous section, the  $\text{HCO}^+$  3–2 line strength can be used to trace the envelope mass uncontaminated by any contribution from a disk, which may be a problem with the 1.1 mm flux. In Fig. 9, the cumulative distribution of the quantity  $\int T_{\text{mb}}dV(\text{HCO}^+ 3-2) / L_{\text{bol}}$  is shown for our nine sources, the five sources from the TGWW sample with weak but detected  $\text{HCO}^+$ , and the sources undetected in  $\text{HCO}^+$ . For this last group, the  $2\sigma$  upper limits are used as if they were detections. The first two groups appear to follow a similar distribution, clearly separated from the third. A Kolmogorov–Smirnov test indicates that there is a chance of  $< 0.2\%$  that the third group is similar to either our sample or the union of the weak- $\text{HCO}^+$  sources with our sample. This difference is based on the strict upper limits acquired on their  $\text{HCO}^+$  3–2 line strengths; it also shows, however, that they do not have the low bolometric luminosity expected from young, but intrinsically low-mass objects. It can therefore be concluded that these sources form a group of more evolved objects than the YSOs selected in §2. The  $\text{HCO}^+$  line strength seems to be a better signpost of young age than either the 1.1 mm continuum flux or the IRAS color.

The assumption of a constant mass-accretion rate is not critical for this conclusion. Two types of variations may exist in  $\dot{M}_{\text{acc}}$ . Firstly, the accretion rate may gradually change over time, and probably decrease (cf. Foster & Chevalier 1993). This results in an enhanced luminosity for young sources and a smaller range in  $M_{\text{env}}/L_{\text{bol}}$ . Since a clear range in  $M_{\text{env}}/L_{\text{bol}}$  is observed, its use as an evolutionary marker is not precluded by this type monotonic of change in  $\dot{M}_{\text{acc}}$ . Secondly, long periods of relatively low accretion rates may be separated by short bursts of high accretion (FU Orionis effect, cf. Hartmann et al. 1993). Protostars are expected to spend  $\sim 10\%$  of their lifetime in a FU Ori phase, which means that only two or three sources of the TGWW sample may be in this phase, and only one of our nine sources. Indeed, L1551 IRS 5 is sometimes referred to as undergoing a FU Ori outburst (Mundt et al. 1985). The effect of the sudden increase in  $L_{\text{bol}}$  is that an object is shifted temporarily to lower  $M_{\text{env}}/L_{\text{bol}}$ ; i.e., it appears more evolved and more massive than it really is. The short period spend in a FU Ori phase, as inferred from the very small number of known FU Ori objects, ensures that for the 24 objects studied here the statistical distribution of  $M_{\text{env}}/L_{\text{bol}}$  is not seriously affected by an individual object undergoing a FU Ori outburst.

A difficulty in using  $\int T_{\text{mb}}dV(\text{HCO}^+ 3-2) / L_{\text{bol}}$  to trace evolution is the opacity of the  $\text{HCO}^+$

3–2 line. In Fig. 9 the cumulative distribution of our sources is shown after taking into account the known 3–2 line opacity (see Table 6). This correction is small for most sources. In addition, it makes the difference between sources detected and undetected in  $\text{HCO}^+$  3–2 larger, strengthening the conclusion that they form two distinct evolutionary groups.

Along the  $\tau$ -corrected curve the position of our objects is indicated, giving a relative evolutionary ordering of our sample. Note that no absolute timescale can be assigned, and that the ordering only reflects how evolved an object is along its route from cloud core to star. Objects of different mass may proceed at different speeds along this track. No correlation is found between either the point-source flux or the ratio of the point-source flux over the total 1.1 mm flux, and the evolutionary phase  $\int T_{\text{mb}} dV(\text{HCO}^+ 3-2) / L_{\text{bol}}$  of our nine sources. This suggests that the mass of the disks does not change significantly during the embedded phase. There is a trend, however, between the point-source flux, the envelope flux, and the luminosity, indicating that the disk flux primarily depends on the mass or activity of the central object.

Myers & Ladd (1993) proposed a diagram of  $L_{\text{bol}}$  versus the bolometric temperature  $T_{\text{bol}}$  as an extension to the Hertzsprung–Russell diagram (the so-called BLT diagram). The quantity  $T_{\text{bol}}$  is defined as the temperature of a blackbody having a maximum at the same frequency as the SED of the source. In Fig. 10 the BLT diagram of the TGWW sample is shown (Chen et al. 1995), with our subsample again indicated by filled symbols. It is seen to populate the upper right-hand region of the diagram, corresponding to young sources. Although no calculations of evolutionary tracks have been published for a BLT diagram yet, a source is expected to proceed from low  $T_{\text{bol}}$  and  $L_{\text{bol}}$  to the main sequence via a maximum in  $L_{\text{bol}}$ . Compared to our evolutionary tracer,  $\int T_{\text{mb}} dV(\text{HCO}^+ 3-2) / L_{\text{bol}}$ , which requires the presence of envelope material, the BLT approach extends over a much larger range in object age. Our method has the advantage, however, that mass and evolution can be separated independent of any collapse model, and that only a sufficiently well-behaved  $\dot{M}_{\text{acc}}$  is required. A more extended survey of  $\text{HCO}^+$  and  $\text{H}^{13}\text{CO}^+$  in a larger variety of objects will therefore be interesting to further investigate this scenario.

## 8. Summary

The envelopes around a sample of nine embedded YSOs have been investigated with 3.4 and 2.7 mm continuum interferometry, and with single-dish observations of the  $\text{HCO}^+$  and  $\text{H}^{13}\text{CO}^+$  1–0, 3–2 and 4–3 transitions. The sources were selected from the IRAS flux and color-limited sample defined by TGWW. The results of this paper can be summarized as follows.

1. Continuum emission at 3.4 and 2.7 mm is detected in the OVRO beam toward all nine sources with integrated fluxes ranging between 4 mJy and 200 mJy. The emission can be described by an unresolved ( $< 3''$ ) point source and, in about half of the objects, emission from an extended, partially resolved envelope. The point-source emission is attributed to thermal dust emission from a circumstellar disk, and its high detection rate suggests that such disks are established already

early in the formation and evolution of protostars. No significant change in the ratio of disk mass over envelope mass is inferred during the subsequent duration of the embedded phase.

2. By extrapolating the point-source fluxes to 1.1 mm, assuming a spectral index  $\alpha = 2.5$ , the relative contributions of the disk and the envelope to the single-dish fluxes observed by Moriarty-Schieven et al. (1994) are estimated. The point sources typically contribute 30–75% to the single-dish flux. The inferred envelope masses within the 19'' JCMT beam are 0.001–0.26  $M_{\odot}$ , assuming an average dust temperature of 30 K.

3.  $\text{HCO}^+$   $J=1-0$  emission maps reveal extended cores ( $> 60''$ ) superposed on emission from the surrounding cloud. In the 3–2 and 4–3 lines the emission is concentrated toward the source positions and marginally resolved ( $\sim 20''$ ), as is expected for a power-law density distribution. The spectra are generally best fit by a narrow emission line ( $\Delta V \approx 2-3 \text{ km s}^{-1}$ ), broad line wings, and, in a few cases, a narrow self-absorption component. The  $\text{H}^{13}\text{CO}^+$  3–2 and 4–3 lines are detected toward half of our sources, with spectra well fit by a single Gaussian at the  $V_{\text{LSR}}$  of the  $\text{HCO}^+$  self-absorption, if present. From observations of  $\text{H}^{13}\text{CO}^+$  1–0 by Mizuno et al. (1994) and  $\text{C}^{18}\text{O}$  1–0 by Hayashi et al. (1994), a beam-averaged  $\text{HCO}^+$  abundance of  $(1.2 \pm 0.4) \times 10^{-8}$  with respect to  $\text{H}_2$  is derived.

4. The 1.1 mm envelope flux and the integrated  $\text{HCO}^+$  line strengths are well correlated, especially for the higher  $J$  transitions. They can both be modeled with the inside-out collapse model of Shu (1977) and with simple power-law density distributions (slopes  $p = 1-3$ ), assuming that the temperature of the dust and the gas has a power law with slope  $-0.4$ , and a value of 30 K at a radius of 1000 AU. Typical densities at  $r = 1000 \text{ AU}$  of  $1 \times 10^4$  to  $2 \times 10^6 \text{ cm}^{-3}$  are inferred. The fact that the models agree well with the observations indicates that  $\text{HCO}^+$  3–2 and 4–3 can be used as envelope tracers, and that no significant depletion of molecules takes place over  $\sim 20''$  scales. However, more detailed comparison with line-profile calculations are required before further constraints can be placed on possible collapse models.

5. Among the remaining objects of the original sample, i.e., those not selected for our subsample, there is a group that have similar 1.1 mm single-dish fluxes compared to our YSOs in spite of undetected  $\text{HCO}^+$  3–2 emission. It is proposed that all their 1.1 mm flux originates in a disk rather than in an extended envelope. Available  $\text{C}^{18}\text{O}$  3–2 and continuum-interferometer data support this interpretation.

6. The quantity  $\int T_{\text{mb}} dV(\text{HCO}^+ 3-2) / L_{\text{bol}}$  is proposed as an evolutionary tracer independent of intrinsic mass, and measures the ratio of the mass of the central star to that of the envelope. It is found that those TGWW sources which are detected in  $\text{HCO}^+$  3–2 have a significantly different distribution in this tracer compared with sources that remain undetected in  $\text{HCO}^+$ . This supports the interpretation of the latter group as more evolved objects, and shows that  $\text{HCO}^+$  is very well suited as a sensitive probe of the early embedded phase of low-mass star formation.

The authors wish to thank Remo Tilanus, Göran Sandell, Fred Baas, and Floris van der Tak

for carrying out part of the JCMT observations. Lee Mundy is acknowledged for useful discussions concerning the analysis of the continuum observations. The staffs of OVRO, JCMT and IRAM 30m are thanked for support during various observing runs. MRH is indebted to the Caltech Divisions of Geological and Planetary Sciences and of Mathematics, Physics and Astronomy, as well as the Owens Valley Radio Observatory for their hospitality. The *Stimuleringsfonds Internationalisering* of the Netherlands Organization for Scientific Research (NWO) and the Leids Kerkhoven–Bosscha Fonds provided travel support for MRH. Research in Astrochemistry in Leiden is supported by NWO/NFRA through grant no. 781–76–015. GAB gratefully acknowledges support provided by NASA grants NAGW–2297 and NAGW–1955, and HJvL support by the European Union under contract CHGECT920011. The referee is thanked for providing insightful comments, which led to a much improved revised manuscript.

## REFERENCES

- Agladze, N. I., Sievers, A. J., Jones, S. A., Burlitch, J. M., & Beckwith, S. V. W. 1994, *Nature*, 372, 243
- André, Ph., & Montmerle, T. 1994, *ApJ*, 420, 837
- Barsony, M., & Kenyon, S. J. 1992, *ApJ*, 384, L53
- Beckwith, S. V. W., Sargent, A. I., Chini, R. S., & Güsten, R. 1990, *AJ*, 99, 924
- Bernes, C. 1979, *A&A*, 73, 67
- Bertout, C. 1983, *A&A*, 126, L1
- Blake, G. A., Laughlin, K. B., Cohen, R. C., Busarow, K. L., & Saykally, R. J. 1987, *ApJ*, 316, L45
- Blake, G. A., van Dishoeck, E. F., Jansen, D. J., Groesbeck, T. D., & Mundy, L. G. 1994, *ApJ*, 428, 680
- Bontemps, S., André, Ph., Terebey, S., & Cabrit, S. 1996, *A&A*, 311, 858
- Boss, A. P. 1993, *ApJ*, 410, 157
- Butner, H. M., Natta, A., & Evans II, N. J. 1994, *ApJ*, 420, 326
- Ceccarelli, C., Hollenbach, D. J., & Tielens, A. G. G.M. 1996, *ApJ*, 471, 400
- Chen, H., Myers, P. C., Ladd, E. F., & Wood, D. O. S. 1995, *ApJ*, 445, 377
- Choi, M. H., Evans II, N. J., Gregersen, E. M., & Wang, Y. S. 1995, *ApJ*, 448, 742
- Dutrey, A., Guilloteau, S., Duvert, G., et al. 1996, *A&A*, 309, 493
- Dutrey, A., Guilloteau, S., Guélin, M. 1997, *A&A*, 317, L55
- Dyck, H. M., Simon, T., & Zuckerman, B. 1982, *ApJ*, 255, L103
- Edwards, S., & Snell, R. L. 1982, *ApJ*, 261, 151
- Fiedler, R. A., & Mouschovias, T. C. 1992, *ApJ*, 391, 199
- Fiedler, R. A., & Mouschovias, T. C. 1993, *ApJ*, 415, 680
- Foster, P. N., & Chevalier, R. A. 1993, *ApJ*, 416, 303
- Fuller, G. A., Ladd, E. F., & Hodapp, K.-W. 1996, *ApJ*, 463, L97
- Galli, D., & Shu, F. H. 1993, *ApJ*, 417, 220
- Ghez, A. M., Neugebauer, G., & Matthews, K. 1993, *AJ*, 106, 2005
- Green, S. 1975, *ApJ*, 201, 366
- Hartmann, L., Kenyon, S., & Hartigan, P. 1993, in *Protostars and Planets III*, eds. E. H. Levy, J. I. Lunine (Tucson: Univ. Arizona), 497
- Hayashi, M., Hasegawa, T., Ohashi, N., & Sunada, K. 1994, *ApJ*, 426, 234

- Hogerheijde, M. R., van Dishoeck, E. F., Blake, G. A., & van Langevelde, H. J. 1998a, in preparation.
- Hogerheijde, M. R., van Langevelde, H. J., Blake, G. A., Mundy, L. G., & van Dishoeck, E. F. 1998b, in preparation.
- Hogerheijde, M. R., et al. 1998c, in preparation.
- Irvine, W. M., Goldsmith, P. F., & Hjalmarsen, Å. 1987, in *Interstellar Processes*, Proc. IAU Symp. 120, eds. D. J. Hollenbach, H. A. Thronson (Dordrecht: Reidel), 561
- Keene, J., & Masson, C. R. 1990, *ApJ*, 355, 635
- Kenyon, S. J., Calvet, N., & Hartmann, L. 1993a, *ApJ*, 414, 676
- Kenyon, S. J., Whitney, B. A., Gomez, M., & Hartmann, L. 1993b, *ApJ*, 414, 773
- Lada, C. J. 1987, in *Star Forming Regions*, eds. M. Peimbert, J. Jugaku (Dordrecht: Reidel), 1
- Ladd, E. F., Adams, F. C., Fuller, G. A., Myers, P. C., Casey, S., Davidson, J. A., Harper, D. A., & Padman, R. 1991, *ApJ*, 382, 555
- Lay, O. P., Carlstrom, J. E., Hills, R. E., & Phillips, T. G. 1994, *ApJ*, 434, L75
- Leinert, C., & Haas, M. 1989, *ApJ*, 342, L39
- Leinert, C., Zinnecker, H., Weitzel, N., Christou, J., Ridgway, S. T., Jameson, R., Haas, M., & Lenzen, R. 1993, *A&A*, 278, 129
- Looney, L. W., Mundy, L. G., & Welch, W. J. 1996, *BAAS*, 189, 53.02
- Millar, T. J., Bennett, A., Rawlings, J. M. C., Brown, P. D., Charnley, S. B. 1991 *A&AS*, 87, 585
- Mizuno, A., Ohishi, T., Hayashi, M., Ohashi, N., Sunada, K., Hasegawa, T., & Fukui, Y. 1994, *Nature*, 368, 719
- Monteiro, T. S. 1985, *MNRAS*, 214, 419
- Moriarty-Schieven, G. H., Wannier, P. G., Tamura, M., & Keene, J. 1992, *ApJ*, 400, 260
- Moriarty-Schieven, G. H., Wannier, P. G., Keene, J., & Tamura, M. 1994, *ApJ*, 436, 800
- Moriarty-Schieven, G. H., Wannier, P. G., Mangum, J. G., Tamura, M., & Olmsted, V. K. 1995, *ApJ*, 455, 190
- Mundt, R., Stocke, J., Strom, S. E., Strom, K. M., Anderson, E. R. 1985 *ApJ*, 297, L41
- Mundy, L. G., Looney, L. W., Erickson, W., Grossman, A., Welch, W. J., Forster, J. R., Wright, M. C. H., Plambeck, R. L., Lugten, J., & Thornton, D. D. 1996, *ApJ*, 464, L169
- Myers, P. C., & Ladd, E. F. 1993, *ApJ*, 413, L47
- Ohashi, N., Kawabe, R., Hayashi, M., & Ishiguro, M. 1991, *AJ*, 102, 2054
- Ohashi, N., Hayashi, M., Kawabe, R., & Ishiguro, M. 1996, *ApJ*, 466, 317
- Ossenkopf, V., & Henning, Th. 1994, *A&A*, 291, 943



- Osterloh, M., & Beckwith, S. V. W. 1995, *ApJ*, 439, 288
- Palla, F., & Stahler, S. W. 1993, *ApJ*, 418, 414
- Pollack, J. B., Hollenbach, D., Beckwith, S. V. W., Simonelli, D. P., Roush, T., & Fong, W. 1994, *ApJ*, 421, 615
- Rodríguez, L. F., Myers, P. C., Cruz-González, I., & Terebey, S. 1989, *ApJ*, 347, 461
- Rowan-Robinson, M. 1980, *ApJS*, 44, 403
- Saraceno, P., André, Ph., Ceccarelli, C., Griffin, M., & Molinari, S. 1996, *A&A*, 309, 827
- Schuster, K. F., Harris, A. I., Andersen, N., & Russel, A. P. G. 1993, *ApJ*, 412, L67
- Scoville, N. Z., Sargent, A. I., Sanders, D. B., Claussen, M. J., Masson, C. R., Lo, K. Y., & Phillips, T. G. 1986, *ApJ*, 303, 416
- Scoville, N. Z., Carlstrom, J. E., Chandler, C. J., Phillips, J. A., Scott, S. L., Tilanus, R. P. J., & Wang, Z. 1993, *PASP*, 105, 1482
- Shu, F. H. 1977, *ApJ*, 214, 488
- Shu, F. H., Najita, J., Galli, D., Ostriker, E., & Lizano, S. 1993, in *Protostars and Planets III*, eds. E. H. Levy, J. I. Lunine (Tucson: Univ. Arizona), 3
- Skinner, S. L., & Brown, A. 1994, *AJ*, 107, 1461
- Stahler, S. W. 1988, *ApJ*, 332, 804
- Tamura, M., Gatley, I., Waller, W., & Werner, M. W. 1991, *ApJ*, 374, L25 (TGWW)
- Terebey, S., Shu, F. H., & Cassen, P. 1984, *ApJ*, 286, 529
- Terebey, S., Vogel, S. N., & Myers, P. C. 1989, *ApJ*, 340, 472
- Terebey, S., Chandler, C. J., & André, Ph. 1993, *ApJ*, 414, 759
- van Dishoeck, E. F., Blake, G. A., Jansen, D. J., & Groesbeck, T. D. 1995, *ApJ*, 447, 760
- van Langevelde, H. J., van Dishoeck, E. F., & Blake, G. A. 1994, *ApJ*, 425, L45
- van Langevelde, H. J., van Dishoeck, E. F., & Blake, G. A. 1997, in *CO: Twenty-five Years of Millimeter-wave Spectroscopy*, Proc. IAU Symp. 170, eds. W. B. Latter et al. (Dordrecht: Kluwer), 469
- Walker, C. K., Lada, C. J., Young, E. T., Maloney, P. R., & Wilking, B. A. 1986, *ApJ*, 309, L47
- Walker, C. K., Narayanan, G., & Boss, A. P. 1994, *ApJ*, 431, 767
- Ward-Thompson, D., Buckley, H. D., Greaves, J. S., et al. 1996, *MNRAS*, 281, L53
- Zhou, S. 1992, *ApJ*, 394, 204
- Zhou, S. 1995, *ApJ*, 442, 685
- Zhou, S., Evans II, N. J., Kömpe, C., & Walmsley, C. M. 1993, *ApJ*, 404, 232

Fig. 1.—  $\text{HCO}^+$  3–2 spectra of the sources defined by Tamura et al. (1991, TGWW) as YSOs (see Table 2). The nine strongest objects selected for further study are shown in the top panel; the others are shown in the lower panel. The vertical scale is antenna temperature  $T_{\text{mb}}$  in K, the horizontal scale is velocity  $V_{\text{LSR}}$  in  $\text{km s}^{-1}$ . The estimated calibration uncertainty of these  $\text{HCO}^+$  3–2 spectra is at least 30%, as discussed in §3.2.

Fig. 2.— In the left-hand panels the vector-averaged,  $uv$ -binned 3.4 and 2.7 mm visibility amplitudes in mJy are plotted against  $uv$  separation in  $k\lambda$ . The observations, indicated by the filled symbols, are shown with their  $1\sigma$  error bars. The dotted line is the zero-signal expectation value, the thick solid line a model fit (see §4.1, Table 4). In the right-hand panels the cleaned images of the 3.4 and 2.7 mm continuum emission are shown, using natural weighting. The beam sizes are indicated in the lower left corner of each panel. The contour levels start at  $2\sigma$  ( $\approx 3 \text{ mJy bm}^{-1}$ ; except for T Tau:  $\sim 10 \text{ mJy bm}^{-1}$  at 3.4 mm,  $\sim 6 \text{ mJy bm}^{-1}$  at 2.7 mm), and increase in steps of  $2\sigma$ .

Fig. 3.— Spectra of  $\text{HCO}^+$  1–0 (bottom), 3–2 (middle), and 4–3 (top curves) toward the nine YSOs of our sample (solid lines). The  $\text{H}^{13}\text{CO}^+$  3–2 and 4–3 spectra are indicated by the dotted lines. The 3–2 and 4–3 spectra are offset by 10 and 20 K respectively; the  $\text{H}^{13}\text{CO}^+$  spectra have been multiplied by a factor of 5 (factor of 10 for L1489 IRS and T Tau; factor of 2.5 for L1551 IRS 5, as indicated). The vertical scale is antenna temperature  $T_{\text{mb}}$  in K, the horizontal scale is velocity  $V_{\text{LSR}}$  in  $\text{km s}^{-1}$ .

Fig. 4.— (a) Contour maps of integrated  $\text{HCO}^+$  1–0 (left-hand panels), 3–2 (upper right-hand panels), and 4–3 (lower right-hand panels) of L1489 IRS, Haro 6–10, L1551 IRS 5, and L1535 IRS. The spectra have been integrated over the full velocity extent of the lines. The positions at which spectra were obtained are indicated by dots, unless the maps are fully sampled at half beam-width intervals. The first contour level and the level increment are  $4\sigma$  for 1–0, and  $2\sigma$  for 3–2 and 4–3. (1–0:  $1.0 \text{ K km s}^{-1}$  for L1489 IRS, Haro 6–10, and L1535 IRS;  $3.0 \text{ K km s}^{-1}$  for L1551 IRS 5. 3–2:  $1.0 \text{ K km s}^{-1}$ . 4–3:  $1.5 \text{ K km s}^{-1}$  for L1489 IRS, Haro 6–10, and L1535 IRS;  $4.5 \text{ K km s}^{-1}$  for L1551 IRS). The 50% intensity contour is indicated by the thick solid line. The respective beam sizes are shown in the lower left corner of each panel. (b) Same for TMR 1, TMC 1A, L1527 IRS, and TMC 1 (1–0:  $4\sigma = 1.0 \text{ K km s}^{-1}$  for TMR 1, TMC 1A, and TMC 1;  $3.0 \text{ K km s}^{-1}$  for L1527 IRS. 3–2:  $2\sigma = 1.0 \text{ K km s}^{-1}$ . 4–3:  $2\sigma = 1.5 \text{ K km s}^{-1}$ .) (c) Same for T Tau. Note that a region of only  $20'' \times 20''$  was mapped in 1–0. (1–0:  $4\sigma = 3.0 \text{ K km s}^{-1}$ . 3–2:  $2\sigma = 3.0 \text{ K km s}^{-1}$ . 4–3:  $2\sigma = 4.5 \text{ K km s}^{-1}$ .)

Fig. 5.— Integrated  $\text{HCO}^+$  (top panels) and  $\text{H}^{13}\text{CO}^+$  (lower panels) 1–0 (left), 3–2 (middle), and 4–3 (right) emission as functions of 1.1 mm envelope flux. The objects of our sample are indicated by the symbols, together with error bars corresponding to the  $\sim 30\%$  calibration uncertainty. The error bar for T Tau in the  $\text{HCO}^+$  4–3 panel also contains the large contribution from the outflow to the line wings. Curves are drawn for the three power-law models, and for the Shu (1977) collapse model. In the  $\text{HCO}^+$  3–2 panel the objects are identified, for comparison with Fig. 8.

Fig. 6.— (a) Continuum flux at 1.1 mm in mJy as function of post-collapse time in yr for the Shu (1977) collapse model. The time at which the collapse expansion wave reaches the outer boundary of the model core is indicated by the dashed line. (b) 1.1 mm flux in mJy as function of  $\text{H}_2$  number density at an arbitrary radius of 1000 AU, for the Shu (1977) collapse model and three power-law density distributions with slopes  $p = 1, 2$  and  $3$ . (c) Integrated intensity of  $\text{HCO}^+$  4–3 (top), 3–2 (middle), and 1–0 (bottom), in  $\text{K km s}^{-1}$ , as functions of density at 1000 AU for the same models, assuming a constant  $\text{HCO}^+$  abundance of  $1.2 \times 10^{-8}$ . (d) FWHM source size, after beam convolution, for  $\text{HCO}^+$  4–3 (top), 3–2 (middle), and 1–0 (bottom) as functions of density at 1000 AU for the same models. The respective beam sizes are indicated by the thick horizontal lines.

Fig. 7.— Integrated intensity in CS 3–2, 5–4 (CSO and JCMT), and 7–6 (from Moriarty-Schieven et al. 1995) against  $\text{HCO}^+$  3–2 for the TGWW source sample. The nine objects investigated in the present paper are indicated by the filled symbols. The size of the symbols corresponds to the uncertainty in the data.

Fig. 8.— Integrated  $\text{HCO}^+$  3–2 against 1.1 mm single-dish flux for the full source sample. The nine objects investigated in the present paper are indicated by the filled symbols. The size of the symbols reflects the uncertainty in the data. Note that, in contrast with the fluxes used in Fig. 5, no correction is made for the contribution of any compact disks. For reference, the curve corresponding to the Shu (1977) collapse model is plotted.

Fig. 9.— Cumulative distribution of  $\int T_{\text{mb}} dV(\text{HCO}^+ 3-2) / L_{\text{bol}}$  of the selected source sample (with and without correction for line opacity), those sources in the TGWW sample which are weak in  $\text{HCO}^+$  3–2, and the sources undetected in  $\text{HCO}^+$  3–2. The sources in the selected sample are identified along the  $\tau$ -corrected curve. The quantity  $\int T_{\text{mb}} dV(\text{HCO}^+ 3-2) / L_{\text{bol}}$  traces  $M_{\text{env}}/M_*$ , i.e., the relative evolutionary phase of an embedded object. Relatively young sources are located on the right of the plot, more evolved ones on the left.

Fig. 10.— Diagram of bolometric luminosity against bolometric temperature (BLT-diagram) of the TGWW source sample. The objects studied in the present paper are indicated by the filled symbols. The main sequence is located at the extreme left of the plot.

Table 1. Selected source sample

Source	IRAS PSC	$\alpha$ (1950.0) <sup>a</sup> h m ss.s	$\delta$ (1950.0) <sup>a</sup> ° ' "	Visible/ Embedded	K mag	NIR <sup>b</sup> slope	$F_{100\mu\text{m}}$ Jy	IRAS <sup>c</sup> color	$L_{\text{bol}}$ $L_{\odot}$	$M_{\star}$ <sup>d</sup> $M_{\odot}$
L1489 IRS	04016+2610	04 01 40.5	+26 10 48	Emb	9.3	2.0	56.0	−0.49	3.70	0.4
T Tau	04190+1924	04 19 04.1	+19 25 06	Vis <sup>e</sup>	(5.4)	0.9	98.1	−0.35	25.50 <sup>f</sup>	2.7 <sup>f</sup>
Haro 6–10	04263+2426	04 26 21.9	+24 26 29	Vis <sup>e</sup>	7.6	2.6	49.3	−0.19	6.98	0.9
L1551 IRS 5	04287+1801	04 28 40.2	+18 01 42	Emb	9.3	2.8	457.9	−0.55	21.90	2.6
L1535 IRS	04325+2402	04 32 33.4	+24 02 13	Emb	11.1	1.8	23.0	−0.79	0.70	0.15
TMR 1	04361+2547	04 36 09.7	+25 47 29	Emb	10.6	2.5	33.1	−0.38	2.90	0.3
TMC 1A	04365+2535	04 36 31.1	+25 35 54	Emb	10.6	2.2	38.0	−0.62	2.20	0.3
L1527 IRS	04368+2557	04 36 49.6	+25 57 21	Emb	(13.0)	2.1	71.0	−1.38	1.30	0.2
TMC 1	04381+2540	04 38 08.4	+25 40 52	Emb	12.0	2.3	12.6	−0.58	0.66	0.15

<sup>a</sup> Best fit positions to 3.4 and 2.7 mm continuum interferometric data (see §4.1).

<sup>b</sup> Near-infrared spectral slope, defined as  $s = d \log S_{\nu} / d \log \lambda$  between 2.2 and 25  $\mu\text{m}$ .

<sup>c</sup> IRAS color, defined as  $\log [F_{\nu}(25 \mu\text{m}) / F_{\nu}(60 \mu\text{m})]$ .

<sup>d</sup> Maximum mass of central object, assuming that all bolometric luminosity is stellar and that the object is on the birthline.

<sup>e</sup> With embedded companion.

<sup>f</sup> Sum of T Tau N and S.

References. — Cohen, Emerson & Beichman 1989 ( $L_{\text{bol}}$  T Tau); Leinert & Haas 1989 (K photometry Haro 6–10); Tamura et al. 1991 (K photometry, NIR slope); Kenyon & Hartmann 1995 ( $L_{\text{bol}}$ ).

Table 2. Full source sample

IRAS PSC	Name	Visual/ Embedded	$T_{\text{eff}}$ K	$L_{\star}$ $L_{\odot}$	$T_{\text{bol}}$ K	$L_{\text{bol}}$ $L_{\odot}$	$F_{\nu}$ (1.1 mm) <sup>a</sup> Jy	HCO <sup>+</sup> 3–2 <sup>a</sup> K km s <sup>–1</sup>
04016+2610	L1489 IRS	Emb	...	...	238	3.70	0.180 ± 0.021	6.90 ± 0.40
04108+2803		Emb	...	...	205	0.72	< 0.1	< 0.25
04113+2758		Emb	...	...	606	2.0	0.461 ± 0.053	< 0.29
04169+2702		Emb	...	...	170	0.80	0.281 ± 0.053	2.10 ± 0.09
04181+2655		Emb	...	...	278	0.43	0.044 ± 0.026	1.10 ± 0.15
04190+1924	T Tau	Vis+Emb	...	...	...	25.50 <sup>b</sup>	0.579 ± 0.027	17.90 ± 0.50
04191+1523		Emb	...	...	...	0.48	0.179 ± 0.027	0.97 ± 0.09
04239+2436		Emb	...	...	236	1.27	0.114 ± 0.021	0.82 ± 0.06
04240+2559	DG Tau	Vis	...	...	1440	6.36	0.523 ± 0.048	< 0.20
04248+2612	HH 31 IRS	Emb	...	...	334	0.36	0.099 ± 0.015	1.90 ± 0.08
04263+2426	Haro 6–10	Vis+Emb	4730	...	253	6.98	0.111 ± 0.011	2.42 ± 0.11
04287+1801	L1551 IRS 5	Emb	...	...	97	21.90	2.77 ± 0.30	9.64 ± 0.22
04288+2417	HK Tau	Vis	3785	1.30	2148	0.81	0.110 ± 0.020	< 0.18
04292+2422	Haro 6–13	Vis	...	...	910	1.30	0.233 ± 0.022	< 0.19
04295+2251	L1536 IRS	Emb	...	...	447	0.44	0.094 ± 0.018	< 0.19
04296+1725	GG Tau	Vis	4060	1.31	2621	2.00	0.74 ± 0.12	< 0.26
04302+2247		Emb	...	...	202	0.34	0.149 ± 0.019	< 0.19
04325+2402	L1535 IRS	Emb	...	...	157	0.70	0.074 ± 0.015	2.30 ± 0.13
04328+2248	HP Tau	Vis	4730	1.22	2748	2.40	< 0.1	< 0.18
04361+2547	TMR 1	Emb	...	...	144	2.90	0.188 ± 0.027	8.20 ± 0.40
04365+2535	TMC 1A	Emb	...	...	172	2.20	0.438 ± 0.038	3.30 ± 0.40
04368+2557	L1527 IRS	Emb	...	...	59	1.30	0.482 ± 0.037	8.80 ± 0.20
04381+2540	TMC 1	Emb	...	...	139	0.66	0.116 ± 0.013	3.20 ± 0.30
04390+2517	LkH $\alpha$ 332/G2	Vis	4060	1.94	2563	1.60	< 0.1	< 0.20

<sup>a</sup> In 19'' beam.

<sup>b</sup> Sum of T Tau N and S. N has  $L_{\text{bol}} = 15.50 L_{\odot}$ ,  $L_{\star} = 7.09 L_{\odot}$ ,  $T_{\text{bol}} = 3452$  K, and  $T_{\text{eff}} = 5250$  K; S has  $L_{\text{bol}} = 10.0 L_{\odot}$  and  $T_{\text{bol}} = 501$  K.

References. — Cohen et al. 1989 ( $L_{\star}$ ); Tamura et al. 1991 (source sample); Moriarty-Schieven et al. 1994 ( $F_{\nu}$ ); Kenyon & Hartmann 1995 ( $T_{\text{eff}}$ ,  $L_{\text{bol}}$ ); Chen et al. 1995, 1997 ( $T_{\text{bol}}$ ,  $L_{\text{bol}}$  04113+2658 and LkH $\alpha$  332/G2); Ohashi et al. 1996 ( $L_{\text{bol}}$  04191+1524).

Table 3. Overview of observations

Year/Month	Instrument	Observation	Sources
1992/4, 1993/7	OVRO	$F_\nu(\lambda = 3.4 \text{ mm})$	T Tau
1993/10, 1994/2–4	OVRO	$F_\nu(\lambda = 3.4 \text{ mm})$	all <sup>a</sup> , except T Tau
1993/1,6	OVRO	$F_\nu(\lambda = 2.7 \text{ mm})$	T Tau
1995/2–5	OVRO	$F_\nu(\lambda = 2.7 \text{ mm})$	Haro 6–10, L1551 IRS 5, L1535 IRS, TMR 1, L1527 IRS, TMC 1
1996/10, 1997/2	OVRO	$F_\nu(\lambda = 2.7 \text{ mm})$	L1489 IRS, TMC 1A
1991/5	IRAM 30m	HCO <sup>+</sup> 1–0	T Tau
1995/5	IRAM 30m	HCO <sup>+</sup> 1–0	all <sup>a</sup> , except T Tau
1993/8	JCMT	HCO <sup>+</sup> 3–2	full source sample (see Table 2)
1995/8	JCMT	HCO <sup>+</sup> 3–2	L1489 IRS, T Tau, TMR 1, TMC 1A, TMC 1
1994/12	JCMT	HCO <sup>+</sup> 4–3	all <sup>a</sup>
1994/12, '95/10, '96/5	JCMT	H <sup>13</sup> CO <sup>+</sup> 3–2, 4–3	all <sup>a</sup>

<sup>a</sup> L1489 IRS, T Tau, Haro 6–10, L1551 IRS 5, L1535 IRS, TMR 1, TMC 1A, L1527 IRS and TMC 1.

Table 4. Fit parameters to millimeter continuum visibilities

Source	$\lambda = 3.4 \text{ mm}$			$\lambda = 2.7 \text{ mm}$			$M_{\text{disk}}^{\text{a}}$ $M_\odot$
	$F_\nu^{\text{point}}$ mJy	$F_\nu^{\text{Gaussian}}$ mJy	FWHM "	$F_\nu^{\text{point}}$ mJy	$F_\nu^{\text{Gaussian}}$ mJy	FWHM "	
L1489 IRS	$4.3 \pm 1.1^{\text{b}}$	...	...	$6.8 \pm 1.3^{\text{b}}$	...	...	$(4.4 \pm 0.7) \times 10^{-3}$
T Tau	$45.6 \pm 5.5$	...	...	$39.1 \pm 4.2$	$35.3 \pm 10.4$	$9 \times 7$	$(2.3 \pm 0.3) \times 10^{-2}$
Haro 6–10	$11.9 \pm 1.7$	...	...	$11.3 \pm 1.4$	$13.7 \pm 4.3$	$7 \times 7$	$(1.0 \pm 0.2) \times 10^{-2}$
L1551 IRS 5	$80.8 \pm 3.0$	$48.3 \pm 10.4$	$10 \times 9$	$97.1 \pm 2.6$	$99.8 \pm 9.3$	$9 \times 7$	$(7.3 \pm 0.2) \times 10^{-2}$
L1535 IRS	$4.6 \pm 1.1^{\text{b}}$	...	...	$6.9 \pm 1.3^{\text{b}}$	...	...	$(4.6 \pm 0.7) \times 10^{-3}$
TMR 1	$10.0 \pm 1.0$	...	...	$12.0 \pm 1.2$	$10.8 \pm 7.6$	$21 \times 3$	$(9.1 \pm 0.6) \times 10^{-3}$
TMC 1A	$18.1 \pm 1.2$	$(21.2 \pm 21.1)$	$(56 \times 15)$	$33.1 \pm 1.3$	...	...	$(2.0 \pm 0.6) \times 10^{-2}$
L1527 IRS	$16.2 \pm 2.2$	$17.9 \pm 3.3$	$8 \times 1$	$26.1 \pm 2.8$	$14.4 \pm 4.9$	$5 \times 1$	$(1.7 \pm 0.1) \times 10^{-2}$
TMC 1	$5.0 \pm 1.1^{\text{b}}$	...	...	$7.6 \pm 1.3^{\text{b}}$	...	...	$(5.0 \pm 0.7) \times 10^{-3}$

<sup>a</sup> Minimum mass of disk assuming optically thin emission and a dust temperature of 30 K (see §4.3).

<sup>b</sup> Doubtful fit: flux close to zero-signal expectation value.

Table 5. Envelope fluxes, masses and densities

Source	$F_\nu$ <sup>a</sup> mJy	$F_\nu^{\text{env}}$ <sup>b</sup> mJy	$M_{\text{env}}$ <sup>c</sup> $M_\odot$	$n_{\text{H}_2}$ <sup>d</sup> $\text{cm}^{-3}$
L1489 IRS	$180 \pm 21$	$112\text{--}180^e$	$0.016\text{--}0.025$	$(0.9\text{--}1.4) \times 10^5$
T Tau	$579 \pm 27$	$211 \pm 47$	$0.029 \pm 0.007$	$(1.6 \pm 0.4) \times 10^5$
Haro 6–10	$111 \pm 11$	$< 30$	$< 0.0042$	$< 2 \times 10^4$
L1551 IRS 5	$2770 \pm 300$	$1875 \pm 300$	$0.26 \pm 0.04$	$(1.8 \pm 0.4) \times 10^6$
L1535 IRS	$74 \pm 15$	$0\text{--}74^e$	$< 0.01$	$< 5.8 \times 10^4$
TMR 1	$188 \pm 27$	$47 \pm 29$	$0.007 \pm 0.004$	$(3.7 \pm 2.2) \times 10^4$
TMC 1A	$438 \pm 38$	$130 \pm 40$	$0.018 \pm 0.006$	$(1.0 \pm 0.3) \times 10^5$
L1527 IRS	$482 \pm 37$	$223 \pm 44$	$0.031 \pm 0.006$	$(1.7 \pm 0.3) \times 10^5$
TMC 1	$116 \pm 13$	$38\text{--}116^e$	$0.005\text{--}0.016$	$(3.0\text{--}9.0) \times 10^4$

<sup>a</sup> 1.1 mm flux from Moriarty-Schieven et al. 1994, Kenyon et al. 1993a.

<sup>b</sup> Envelope flux, corrected for contribution from the disk, see Table 4.

<sup>c</sup> Mass in  $19''$  beam, see §4.3.

<sup>d</sup> Density at arbitrary radius  $r = 1000$  AU, see §6.

<sup>e</sup> No constraints on spatial distribution of flux in OVRO beam; indicated range corresponds to the assumption that all, respectively none, of the OVRO flux originates in a disk.

Table 6. HCO<sup>+</sup> line intensities, opacities and source sizes

Source	$I_{1-0}$ <sup>a</sup> K km s <sup>-1</sup>	$\theta_{1-0}$ <sup>b</sup> "	$\bar{\tau}_{1-0}$ <sup>c</sup>	$I_{3-2}$ K km s <sup>-1</sup>	$\theta_{3-2}$ "	$\bar{\tau}_{3-2}$	$I_{4-3}$ K km s <sup>-1</sup>	$\theta_{4-3}$ "	$\bar{\tau}_{4-3}$
HCO <sup>+</sup>									
L1489 IRS	6.7 ± 0.2	60	...	6.9 ± 0.4	24	6.8 ± 1.2	10.0 ± 0.3	17	4.0 ± 0.5
T Tau	16.6 ± 0.2	... <sup>h</sup>	...	17.9 ± 0.5 <sup>d</sup>	25	2.3 ± 0.4	37.1 ± 0.5 <sup>e</sup>	20	3.3 ± 3.1
Haro 6–10	2.8 ± 0.1	90	...	2.4 ± 0.1 <sup>f</sup>	... <sup>f</sup>	< 5.3	5.4 ± 0.5	23	< 3.0
L1551 IRS 5	9.2 ± 0.3	140	12.2 ± 0.9	9.6 ± 0.2 <sup>f</sup>	... <sup>f</sup>	12.7 ± 2.2	22.7 ± 0.4	22	6.8 ± 0.5
L1535 IRS	7.0 ± 0.1	110	9.0 ± 0.6	2.3 ± 0.1 <sup>f</sup>	... <sup>f</sup>	< 6.3	3.0 ± 0.7	24	< 7.8
TMR 1	4.3 ± 0.1	48	12.0 ± 1.2	8.2 ± 0.4	30	4.1 ± 0.6	7.3 ± 0.7	24	< 1.6
TMC 1A	2.2 ± 0.1	75 <sup>h</sup>	20.9 ± 3.5	3.3 ± 0.4	19	< 6.3	3.5 ± 0.4	20 <sup>h</sup>	< 2.6
L1527 IRS	6.5 ± 0.3	63	17.9 ± 1.6	8.9 ± 0.2 <sup>f</sup>	... <sup>f</sup>	6.7 ± 0.7	12.9 ± 0.7	... <sup>i</sup>	1.3 ± 0.4
TMC 1	2.2 ± 0.1	66	...	3.2 ± 0.3	26	< 6.3	5.5 ± 0.7	19	< 1.1
H <sup>13</sup> CO <sup>+</sup>									
L1489 IRS	...	...	...	0.67 ± 0.07	...	...	0.61 ± 0.05	...	...
T Tau	...	...	...	0.69 ± 0.07	...	...	0.58 ± 0.05	...	...
Haro 6–10	...	...	...	< 0.27	...	...	< 0.23	...	...
L1551 IRS 5	1.57 ± 0.05	...	...	2.41 ± 0.3	...	...	2.23 ± 0.1	...	...
L1535 IRS	0.89 ± 0.04 <sup>g</sup>	...	...	< 0.27	...	...	< 0.26	...	...
TMR 1	0.72 ± 0.05	...	...	0.50 ± 0.05	...	...	< 0.20	...	...
TMC 1A	0.60 ± 0.04	...	...	< 0.27	...	...	< 0.13	...	...
L1527 IRS	1.56 ± 0.05	...	...	1.24 ± 0.2	...	...	0.35 ± 0.03	...	...
TMC 1	...	...	...	< 0.27	...	...	< 0.12	...	...

<sup>a</sup>  $I_{u-l}$ : integrated intensity  $\int T_{mb} dV$  of transition  $u-l$ .

<sup>b</sup>  $\theta_{u-l}$ : FWHM source size.

<sup>c</sup>  $\bar{\tau}_{u-l}$ : opacity averaged over line profile assuming an abundance ratio of 65:1 for [HCO<sup>+</sup>]:[H<sup>13</sup>CO<sup>+</sup>].

<sup>d</sup> At (0'', -5''); no significant contribution from outflow.

<sup>e</sup> Contribution of outflow to intensity integrated over 0–14 km s<sup>-1</sup> is  $\sim 30$  K km s<sup>-1</sup>.

<sup>f</sup> JCMT August 1993: calibration uncertain by 30%, no map obtained.

<sup>g</sup> No line width given;  $\Delta V = 0.6$  km s<sup>-1</sup> adopted.

<sup>h</sup> Extent of emission ill defined.

<sup>i</sup> No map obtained.

References. — Mizuno et al. 1994 (H<sup>13</sup>CO<sup>+</sup> 1–0, assuming  $\eta_{mb} = 1.0$ ).



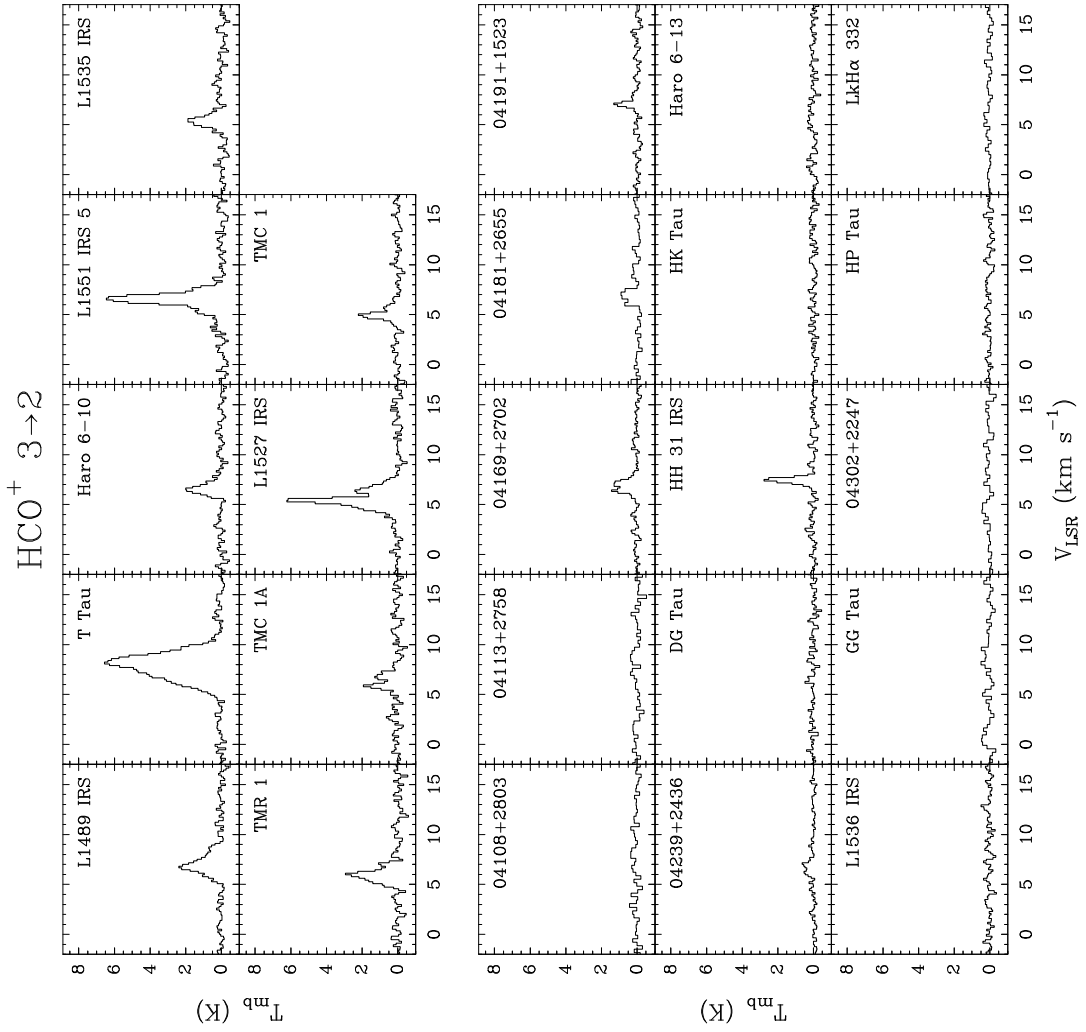


Fig. 1

Fig. 2a

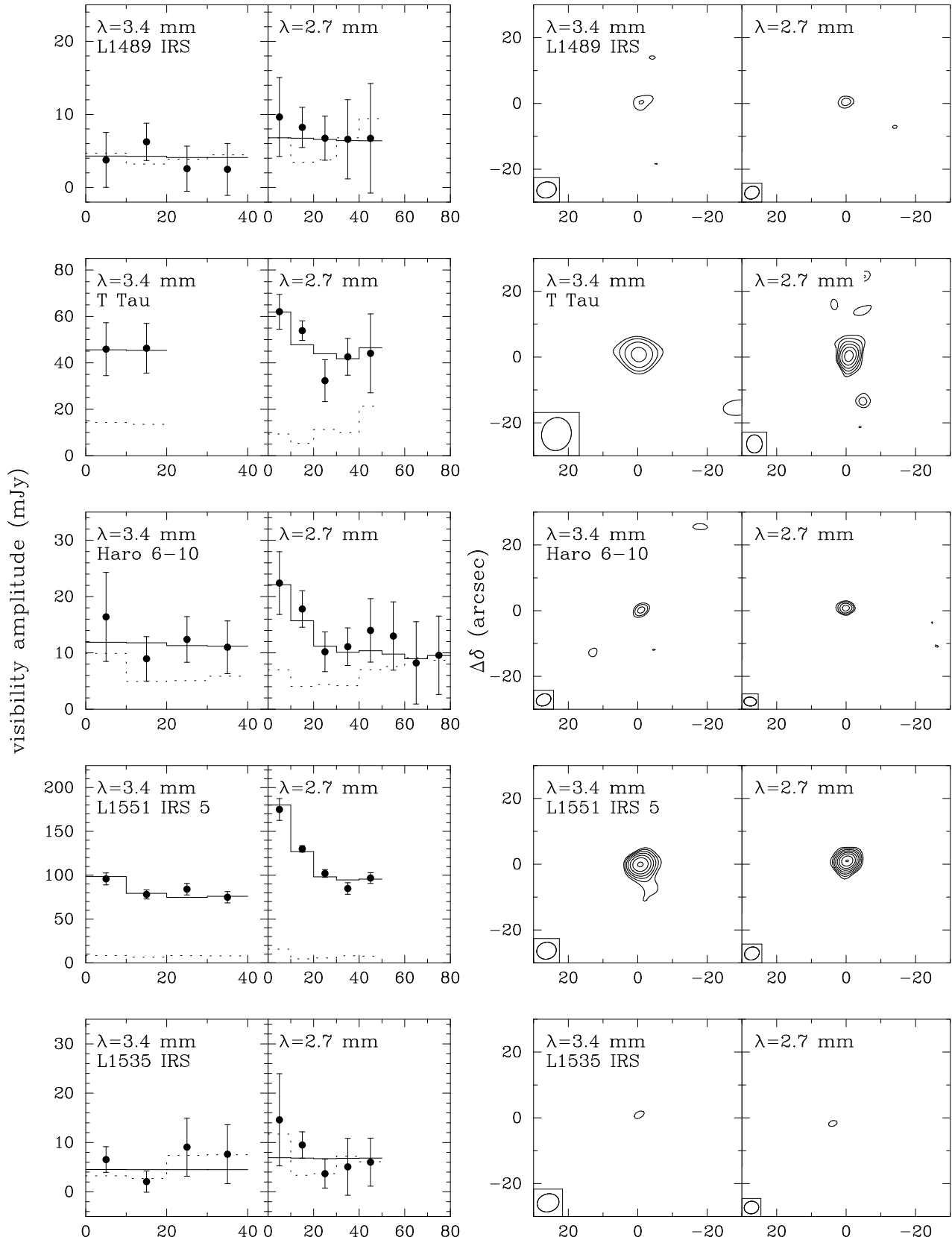
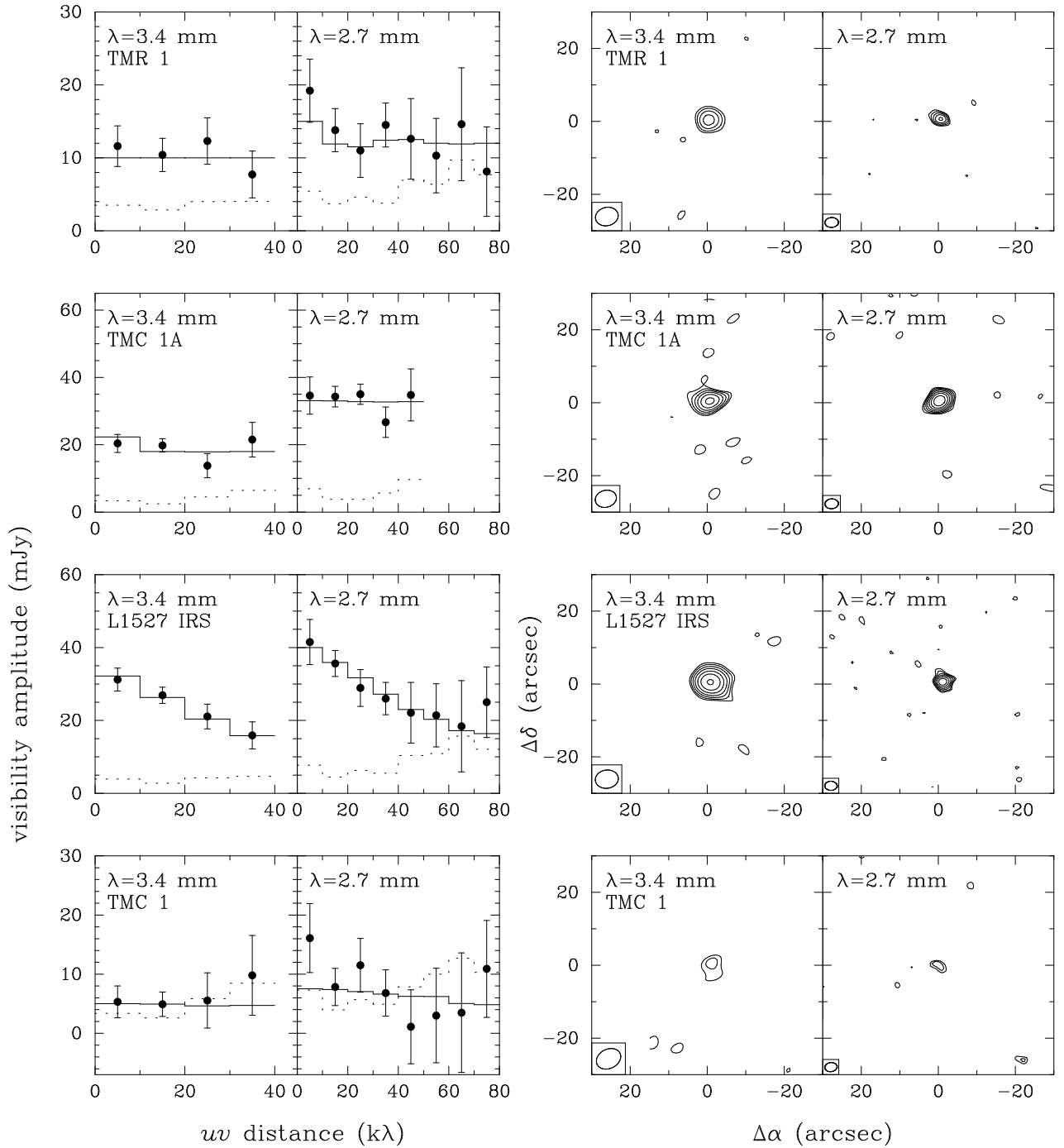


Fig. 2b



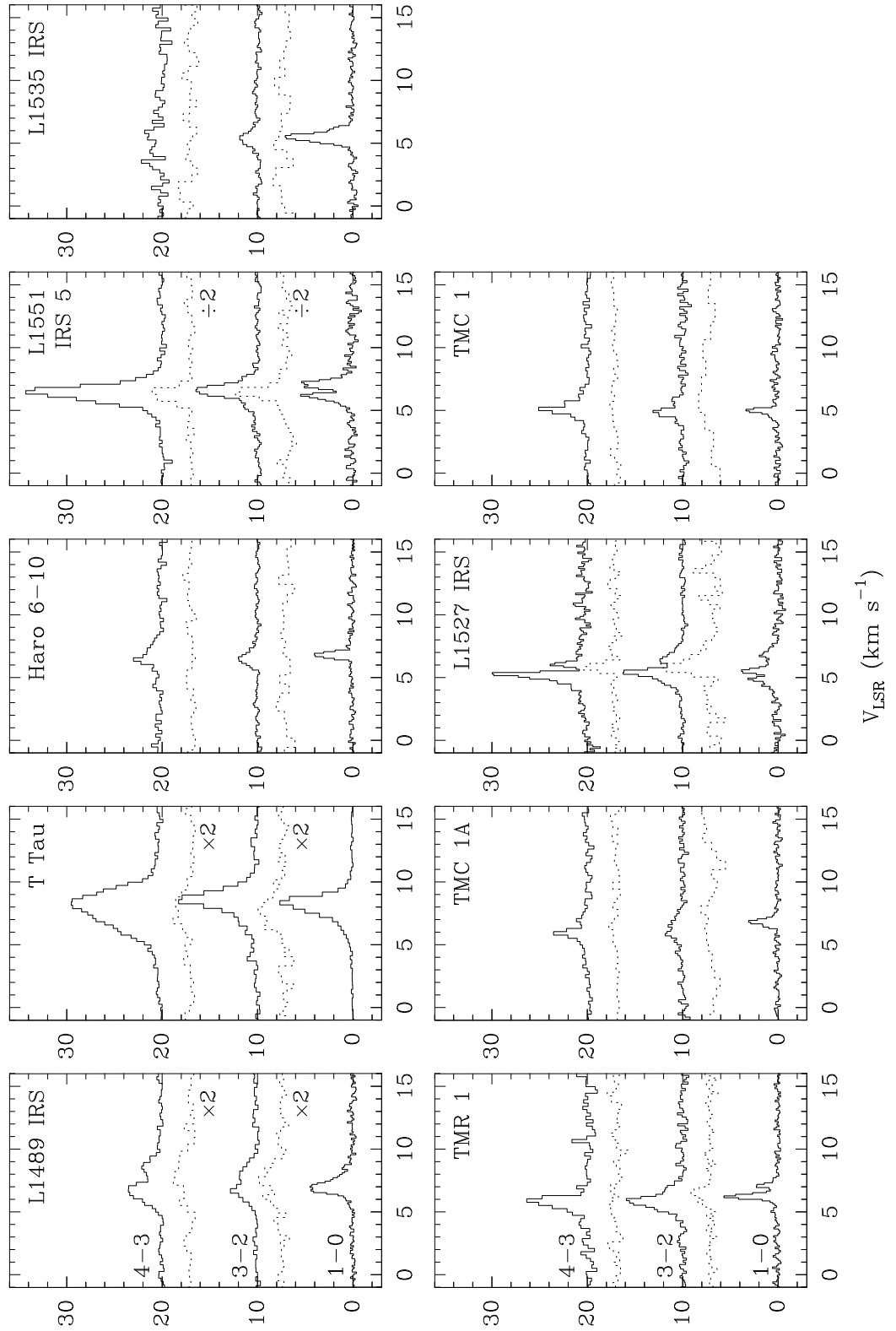


Fig. 3

Fig. 4a

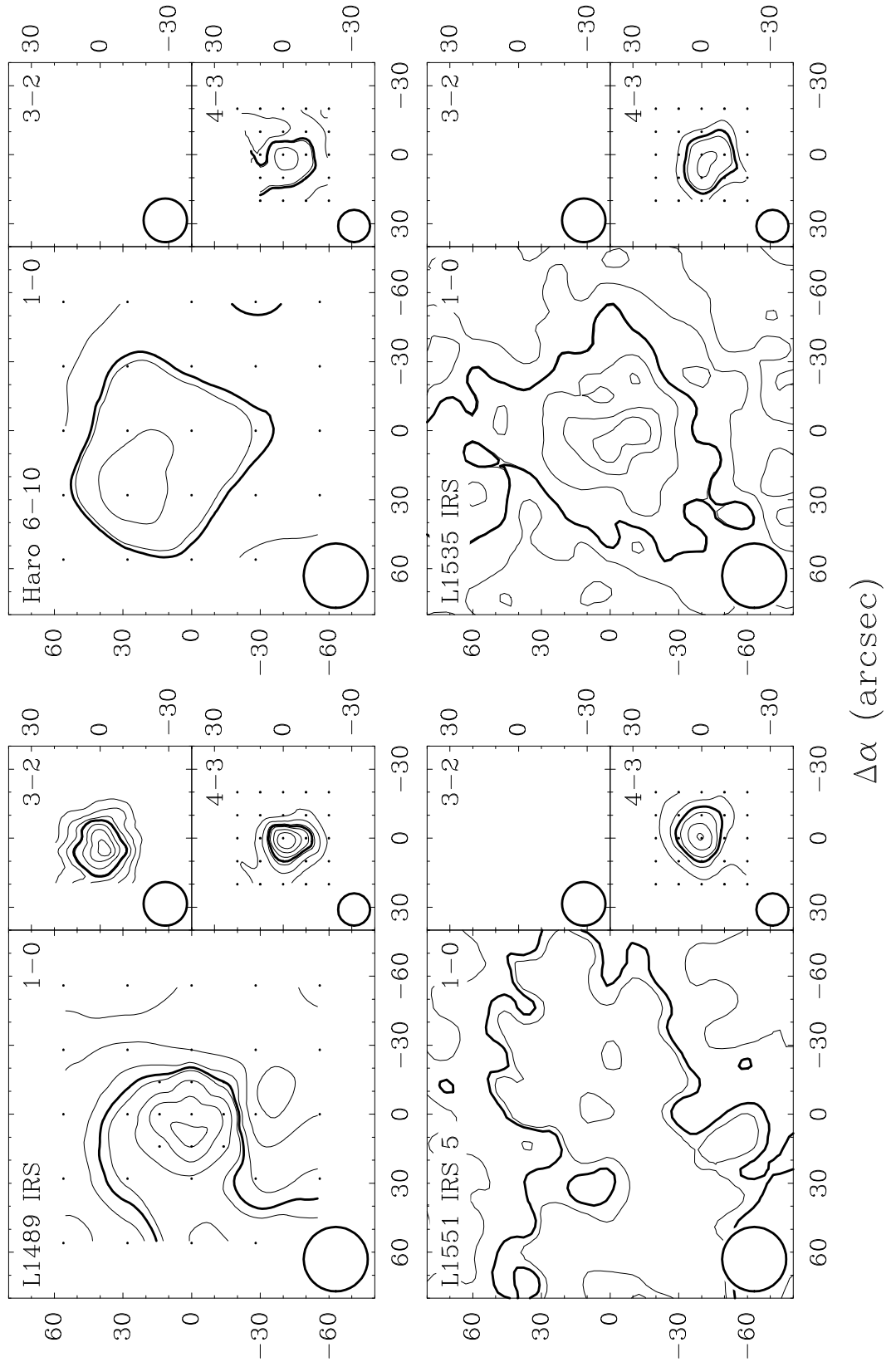


Fig. 4b

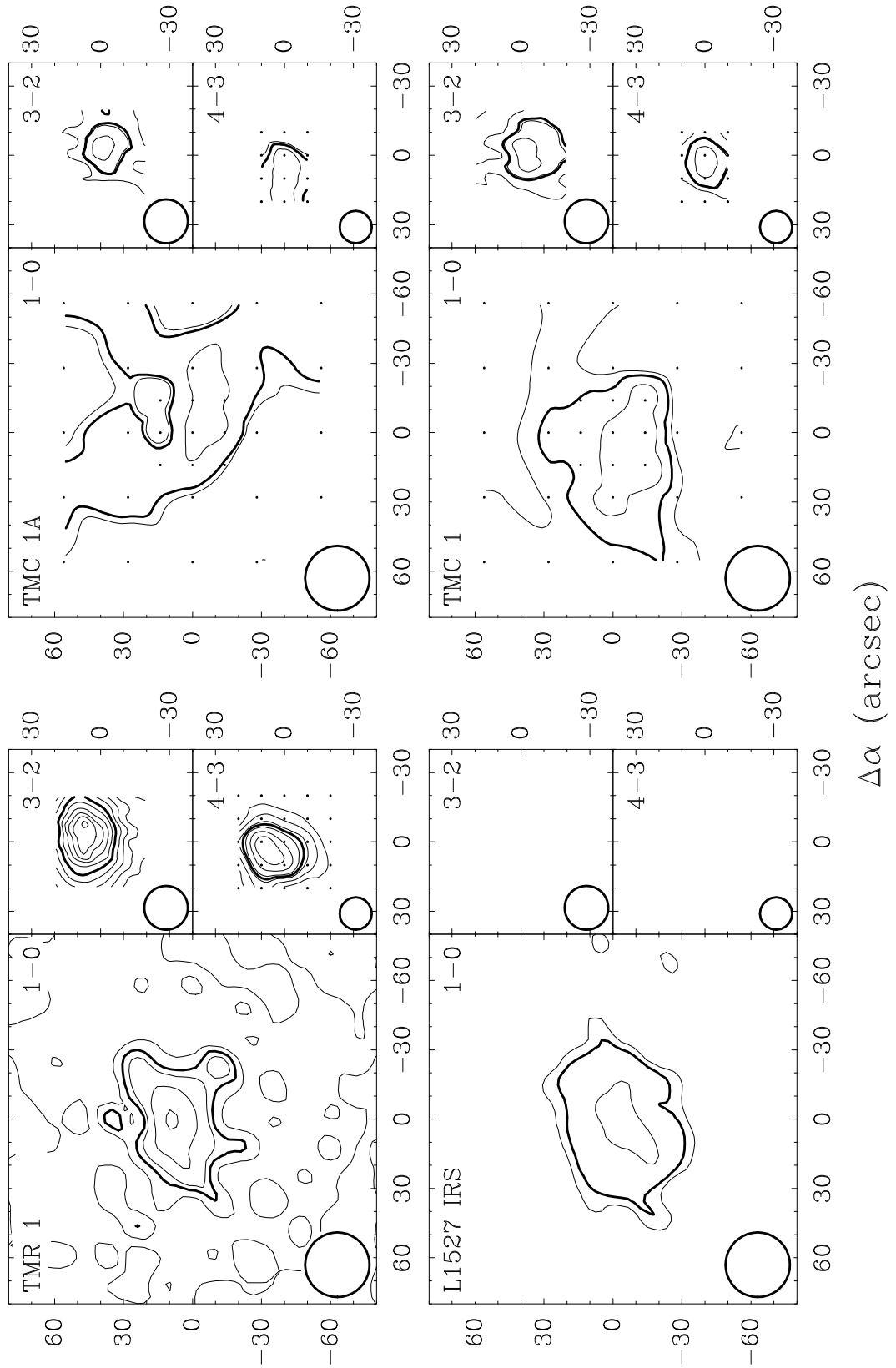
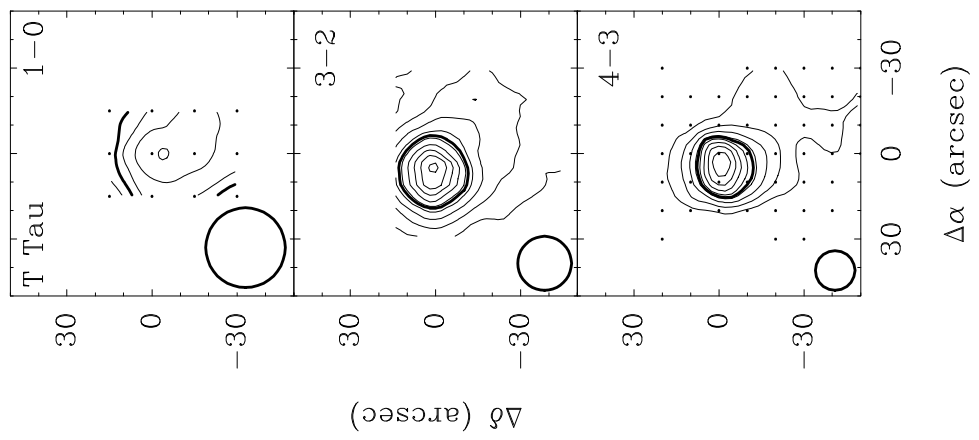


Fig. 4c



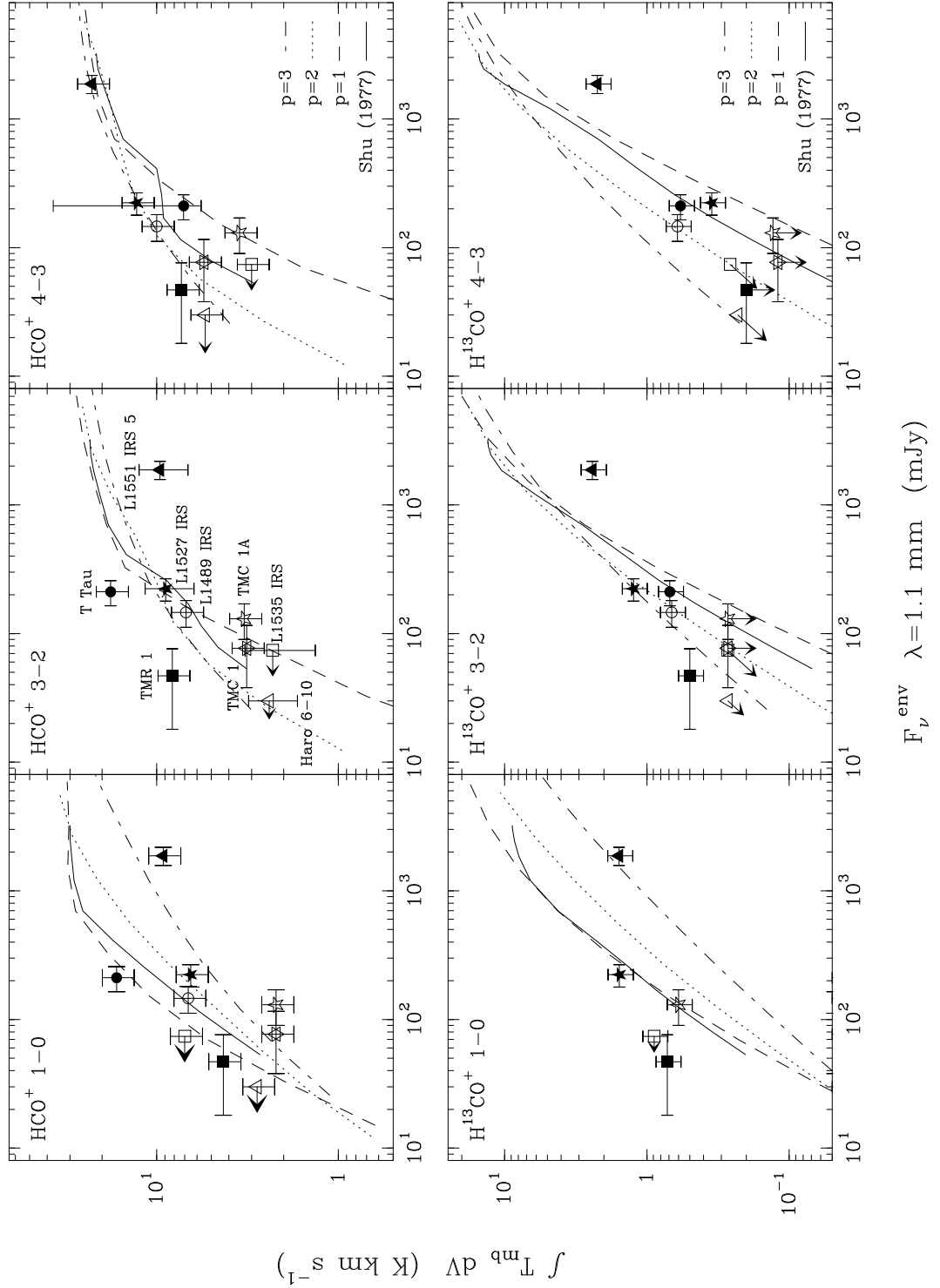


Fig. 5



Fig. 6

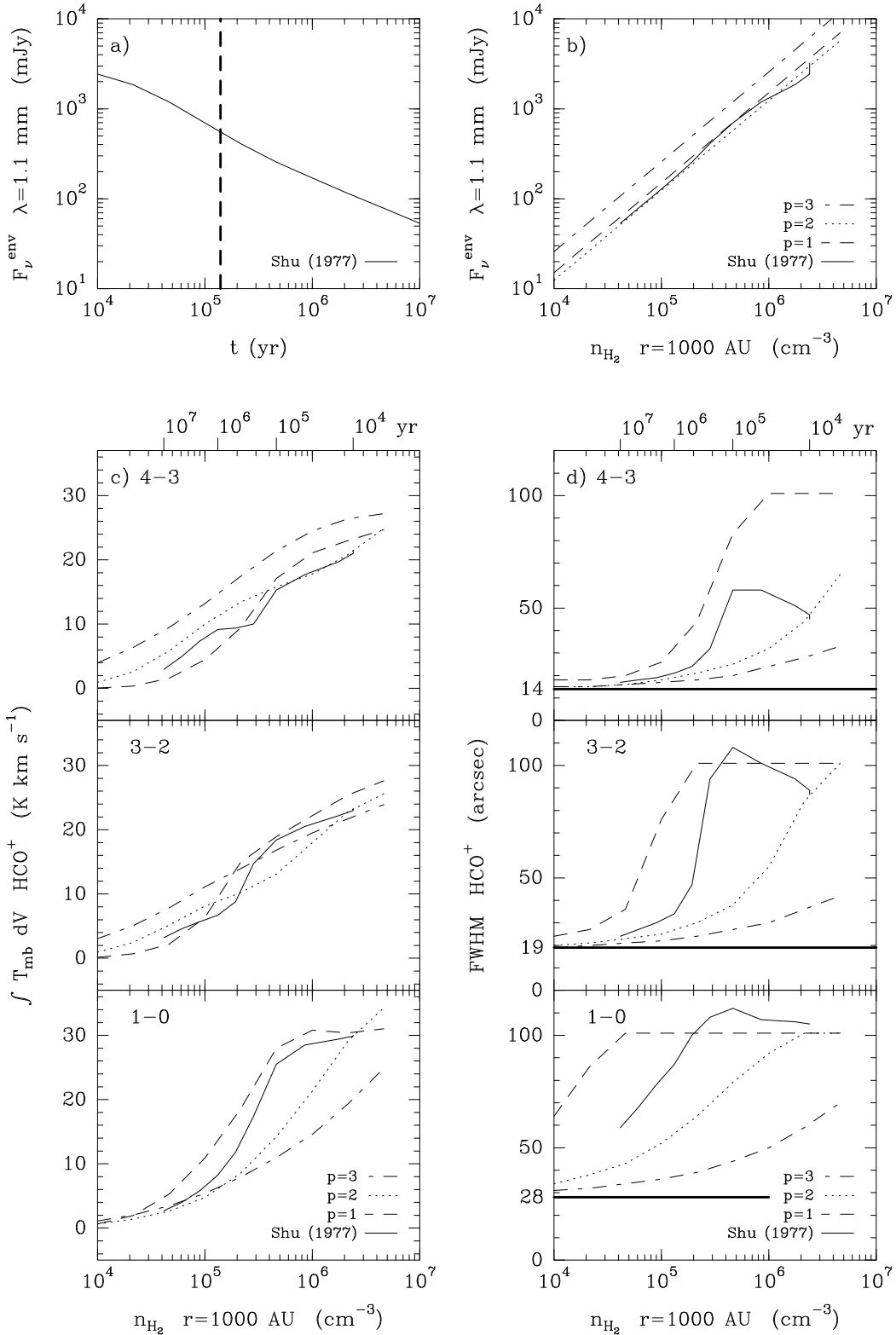


Fig. 7

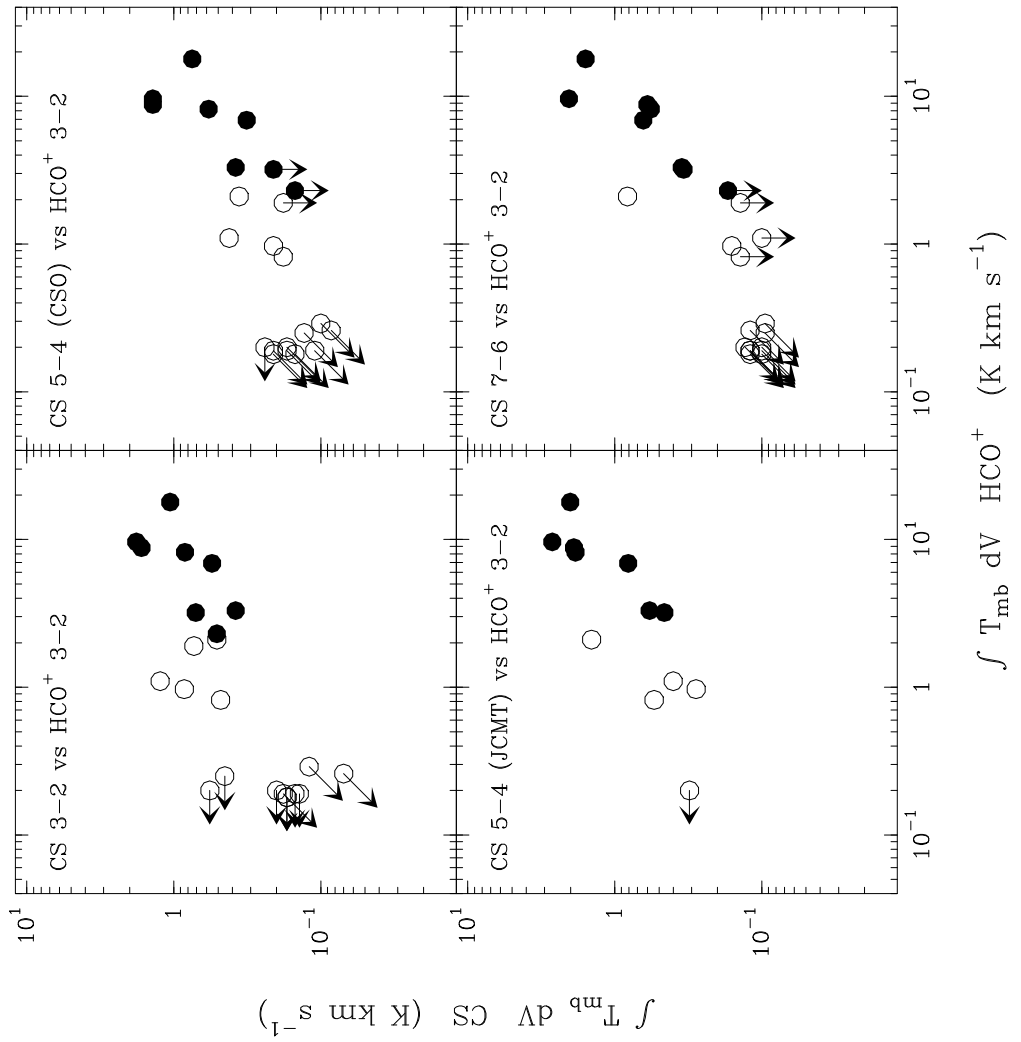


Fig. 8

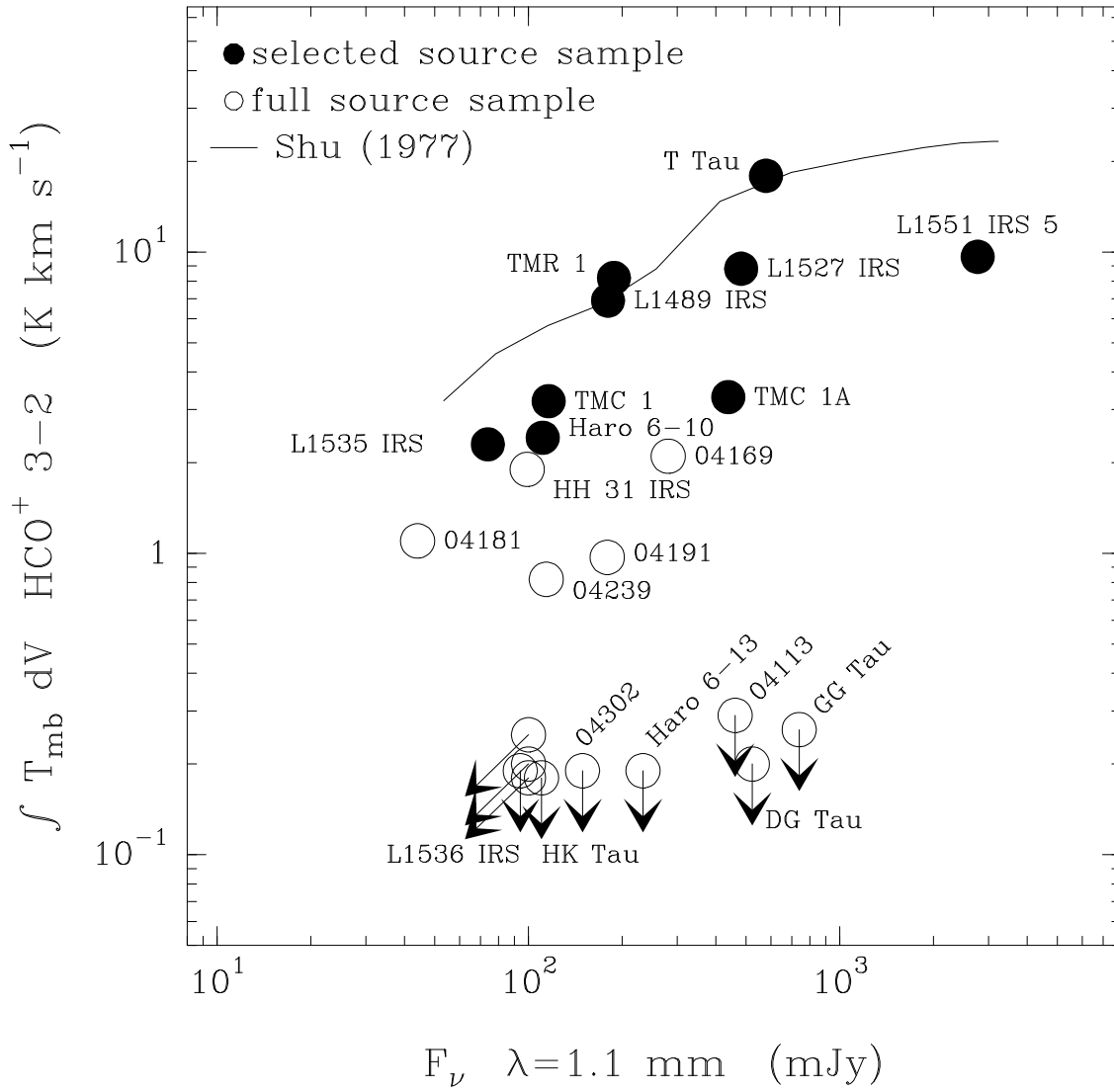


Fig. 9

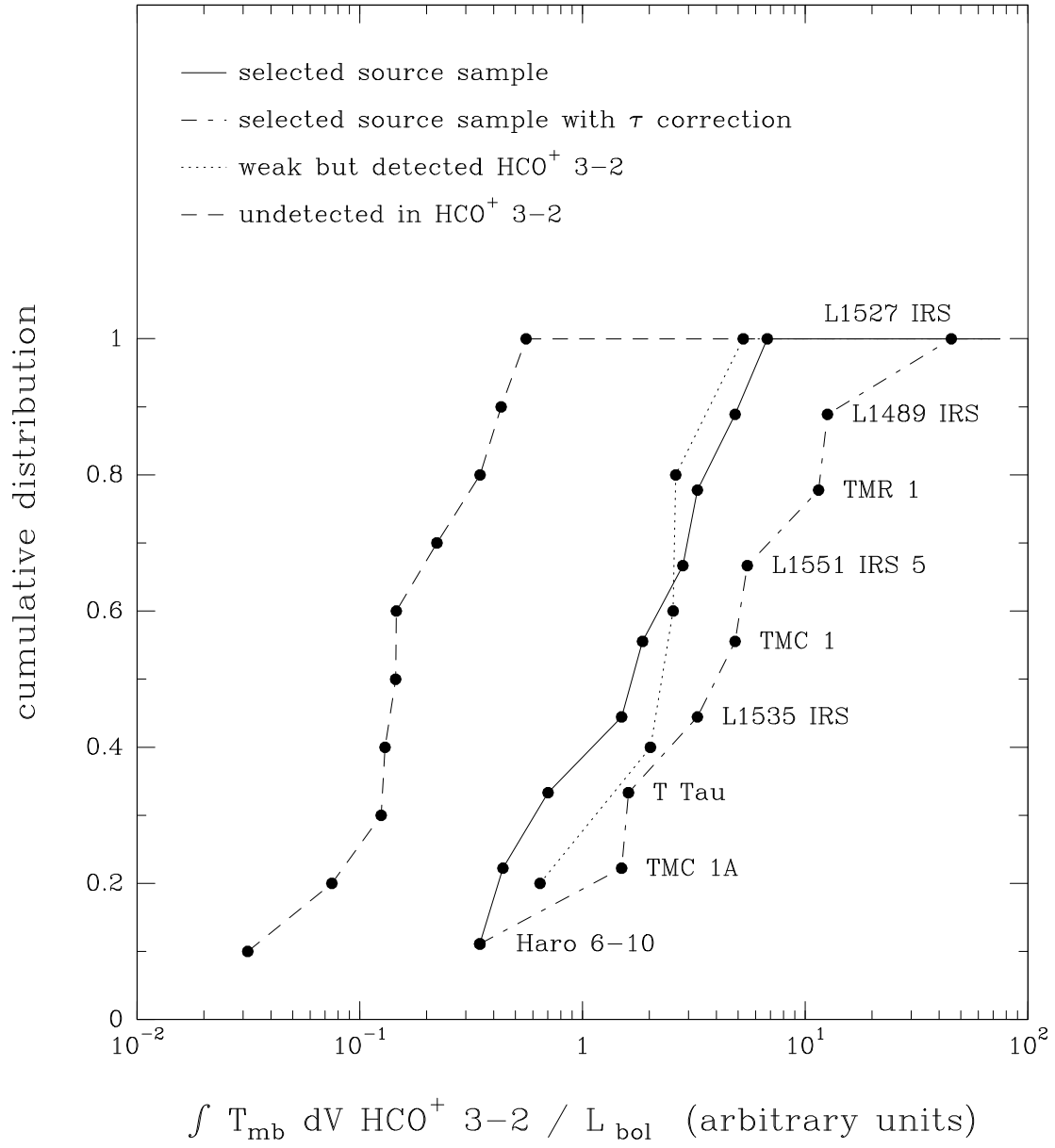


Fig. 10

